Hydrodynamic analysis of resonant waves within the gap between a vessel and a vertical quay wall

Cong, Peiwen
State Key Laboratory of Coastal and Offshore Engineering, Dalian University of Technology

Teng, Bin
State Key Laboratory of Coastal and Offshore Engineering, Dalian University of Technology

Gou, Ying
State Key Laboratory of Coastal and Offshore Engineering, Dalian University of Technology

Tan, Lei
Research Institute for Applied Mechanics, Kyushu University

他

出版情報：Ocean Engineering. 260, pp.112192-, 2022-09-15. Elsevier
バージョン：
権利関係：

Hydrodynamic analysis of resonant waves within the gap between a vessel and a vertical quay wall

Peiwen Cong[a], Bin Teng[a], Ying Gou[a]*, Lei Tan[b], Yingyi Liu[b]

[a] State Key Laboratory of Coastal and Offshore Engineering, Dalian University of Technology, Dalian 116024, China

[b] Research Institute for Applied Mechanics, Kyushu University, Fukuoka 8168580, Japan

Abstract

Concerning the side-by-side offloading operations at gravity-based terminals, the wave interaction with a vessel alongside a long vertical wall in both normal and oblique seas was investigated. The imaging principle was applied to convert the original to an equivalent wave-diffraction problem by two symmetrical vessels in open seas exposed to bi-directional incident waves. The boundary integral equation method, in conjunction with a higher-order boundary element method (HOBEM), was used to solve the equivalent problem. Besides the linear free-surface elevation and wave force, the second-order mean wave drift force on the vessel was calculated based on either the direct pressure integration or using a semi-cylindrical control surface. Moreover, the solution was also developed for the oblique wave interaction with a two-dimensional barge-wall system using the eigenfunction expansion matching method. Systemic numerical studies were then conducted for the cases of a rectangular barge and a Wigley hull in close proximity to a long wall, respectively. Under oblique incidence, both the odd and even modes of fluid motion within the gap can be induced. In the case of a rectangular barge, the linear wave force can be obviously enhanced at the location of the (1, 0) resonant mode, while the linear wave moment at (2, 0) mode. In addition, the negative mean force along the transverse direction, which tends to push the barge away from the wall, can be evidently enhanced at either the odd or even resonant modes. Besides, in oblique seas, the (1, 0) resonant mode can apparently amplify the positive mean yaw moment on the barge, which tends to pull the stern of the barge (that faces

incident waves) closer to the wall, while pushing the bow away from the wall. Numerical results also indicate that the hull geometry imposes a significant impact on the resonant waves in the gap. In the case of a Wigley hull, the amplification of the free-surface response is much less apparent when compared with a rectangular barge.

Key Words:

Narrow gap; oblique seas; mean wave drift force and moment; rectangular barge; Wigley hull; resonant modes

1. Introduction

In recent years, the hydrodynamic interaction between multiple structures in close proximity has been receiving increasing attention. This is primarily because of the possible violent fluid motion within the narrow gap between the closely spaced bodies. In reality, this is a key technical challenge for the safe operation of many side-by-side scenarios, such as a floating liquefied natural gas (FLNG) facility alongside a liquefied natural gas (LNG) carrier or shuttle tanker. Similar phenomena may also exist in the narrow gap formed by an LNG carrier and a gravity-based wharf. The resonant fluid motion in a narrow gap is a weakly damped hydrodynamic phenomenon and normally referred to as “gap resonance”. This hydrodynamic issue may hinder the offshore loading/offloading operation and seriously threaten the structural safety. Therefore, enhancing the knowledge of the exaggerated free-surface oscillation in the narrow gap and understanding its fundamental physics is important for engineering practice.

The wave interaction with floating bodies in a side-by-side arrangement has been investigated in a variety of works ranging from analytical studies (Miao et al., 2001; Liu and Falzarano, 2019) to model scale testing (Molin et al, 2009; Zhao et al, 2017; Ning et al., 2018; Zhou et al., 2018) and numerical modelling (Lu et al, 2010; Feng et al, 2015; He et al., 2021). Based on the potential flow theory, both the two-dimensional

and three-dimensional numerical models have been developed. The piston- and sloshing-model wave resonance along the transverse and longitudinal directions of the narrow gap have been simulated (Sun et al., 2010; Sun et al., 2015; Tan et al., 2019; Li et al., 2021; Ding et al., 2022), and the effect of the wave nonlinearity on the resonant fluid motion and the resulting wave force on the bodies have been discussed for both the monochromatic and bi-chromatic sea conditions (Feng et al., 2017; Zhao et al., 2021). Extensive comparisons with the experimental data have demonstrated that the classical potential flow model can well predict the resonant frequency. However, it was reported to evidently overestimate the resonant free-surface elevation in the narrow gap when compared with the laboratory observations, such as in Saitoh et al. (2003), Faltinsen et al. (2007), and Perić and Swan (2015). To address this issue, special numerical techniques have been proposed, for example, introducing an artificial dissipation layer on the free surface in the gap (e.g., Pauw et al., 2007; Bunnik et al., 2009) or inside the fluid domain at the gap entrance (e.g., Liu et al., 2020; Liang et al., 2021) to consider linear and/or nonlinear damping. However, it remains challenging to reasonably determine the quadratic damping due to flow separations without available experimental data or established empirical formulae. Besides the potential flow model, the CFD-based viscous flow model has gradually become an effective tool for the research of gap resonance (Kristiansen and Faltinsen, 2010; Lu et al., 2011). The existing studies based on viscous flow models focus on two-dimensional configurations subjected to the normally-incident waves. Numerical studies have been conducted for various edge profiles of gap entrance. The effects of the vortical motion and vortex shedding on the resonant response have been discussed.

Besides the problems of gap resonance involving two floating bodies in a side-by-side arrangement, the scenarios that a ship or an LNG carrier berthing in front of a gravity-based wharf have also been investigated in many studies. Wang and Zou (2007) established a two-dimensional time-domain numerical model based on the Boussinesq equations, in which Newton's second law has been used to solve the piston mode of the free-surface motion within the gap between a ship section and a vertical quay wall. It

was found that when the frequency of the linear or higher-order harmonic components of the incident waves is close to the natural frequency of the fluid motion in the gap, the horizontal wave force on the ship's section is greatly increased. A similar two-dimensional setting has been concerned in Kristiansen and Faltinsen (2010), and numerical results indicated that the majority of energy dissipation occurs around the bilge keels of the ship. Peric and Swan (2015) experimentally studied the spatial variation of the free-surface elevation within the long gap formed by a gravity-based structure and a nearby ship in beam-sea and head-sea orientation. Amplification of the free-surface elevation that reaches six times the incident wave amplitude has been observed. Jiang et al. (2019, 2021) investigated the behaviour of the piston-modal wave resonance excited by the linear and second harmonic components of incident waves for a two-dimensional barge-wall system based on the OpenFOAM® package. The effect of seabed slope on the wave force on a fixed box in front of a vertical wall and the free-surface elevation in the gap have been studied in detail in Gao et al. (2019, 2020). Liu et al. (2020) developed a dissipative semi-analytical solution for the wave action on a rectangular box in front of a wall. The comparison with the experimental data illustrated that the introduction of a quadratic pressure loss condition on the gap entrance can be an effective manner to account for the damping effect, and a formula for predicting the energy loss coefficient was developed. Lu et al. (2020) focused on the conditions that a swaying or heaving body located in close proximity to a vertical wall and found that the wave amplitude during the gap resonance can be reduced by the body motion. Such reduction is strongly dependent on the mooring stiffness. He et al. (2021) conducted the harmonic analysis of resonant wave height in the gap formed by a box and a wall, and found that the relative importance of the high-order components increases gradually with the incident wave height. Milne et al. (2022) experimentally studied the wave-induced resonant flow motion in a narrow gap between a vertical wall and a stationary hull and demonstrated that the energy dissipation around the bilge keels causes a quadratically damped free-surface response.

The wave interaction with a barge-wall system, which approximates the scenario that

an LNG carrier is alongside a gravity-based wharf, has been thoroughly investigated in the recent past. However, most of these works focused on two-dimensional cases and normally-incident waves. To the best of the authors' knowledge, the studies involving a three-dimensional system have not been conducted so far, and the effect of wave heading has rarely been discussed. To fill this gap, the wave interaction with a three-dimensional system involving a vessel and a long vertical wall was investigated in this study. Both the normal and oblique sea conditions have been considered. The vertical wall is assumed to be fully reflective and infinitely long. A numerical approach was then developed using HOBEM in conjunction with the imaging principle. Moreover, for the oblique wave interaction with a two-dimensional barge-wall system, which can be regarded as a limiting case as the barge length tends to infinity, the solution was developed using the eigenfunction expansion matching method. After confirming the validity of the developed model, detailed numerical studies were conducted for both cases of a rectangular barge and a Wigley hull in close proximity to a long wall, respectively. The free-surface response in the gap, as well as the induced wave force on the vessel, were discussed.

The remaining part of this paper is organized as follows. The development of the numerical model is introduced in detail in Section 2, which is followed by the calculation of the free-surface elevation in the gap and the wave force on the vessel. After examining the validity of the developed model in Section 4, numerical studies are conducted in detail in Section 5. Finally, conclusions are drawn in Section 6.

2. A numerical approach for the wave interaction with a vessel alongside a vertical wall

The wave interaction with a three-dimensional vessel in front of a vertical wall at a constant water depth h is considered. Fig. 1 shows the definition sketch for this problem, in which a rectangular barge and a Wigley hull have been taken as examples, respectively. As shown in Fig. 1, the vessels are of length l, width b and draft d. The gap width between the vessel and the vertical wall is e. The closeness of the vessel and

the vertical wall leads to the formation of a long and relatively narrow gap. The vessel is exposed to the plane incident waves of angular frequency ω and wave amplitude A. A global Cartesian coordinate system ($Oxyz$) is adopted with an origin located on the still free surface. The z-axis is defined as positive upwards, and the Oyz plane coincides with the vertical wall. The incident waves propagate at an angle of β with respect to the positive x-axis. It is assumed that the vertical wall is infinitely long and fully reflective. By applying the imaging principle (Teng et al., 2004), the original hydrodynamic problem is then transformed into an equivalent one in the open fluid domain in which the real vessel and its virtual image with respect to the wall are exposed to the dual incident waves without the presence of the wall. One of the dual incident waves propagates at an angle of β, and the other, hence, at an angle of $(\pi - \beta)$. The definition sketch for the equivalent problem in open seas is shown in Fig. 2.

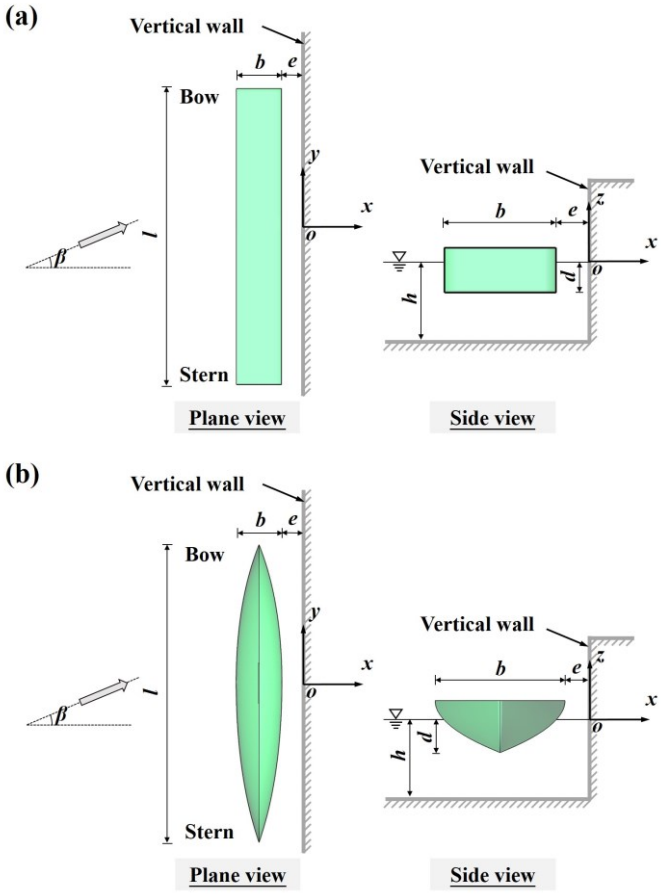

Fig. 1. Definition sketch for (a) a rectangular barge and (b) a Wigley hull near a vertical wall

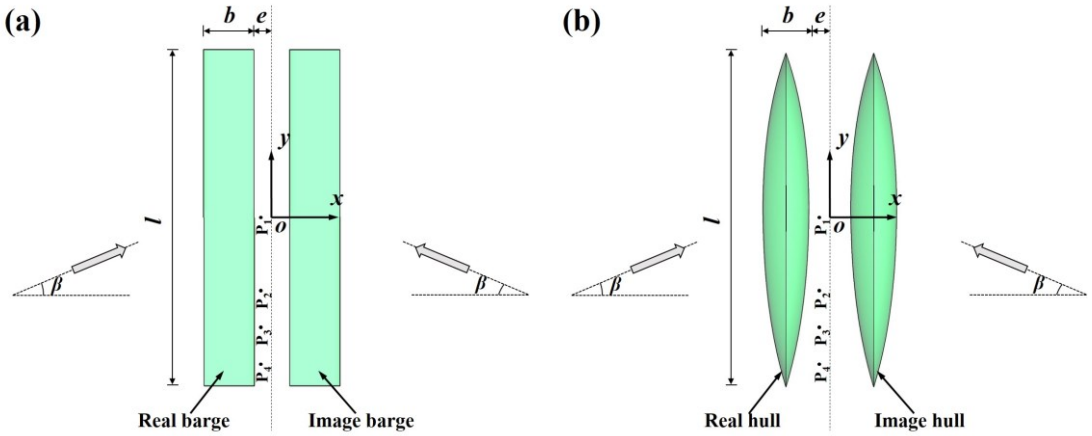

Fig. 2. Plane view of the bi-directional wave action with two symmetrical (a) rectangular barges and (b) Wigley hulls in open seas.

The equivalent problem in the open fluid domain under the action of dual incident waves is then considered. Within the framework of potential flow theory, in which the flow is assumed to be inviscid, incompressible and irrotational, the flow field can be described by a scalar velocity potential Φ, satisfying Laplace's equation

$$\nabla^2\Phi(\mathbf{x};\,t)=0. \tag{1}$$

For linear time-harmonic incident waves with an angular frequency of ω, the velocity potential can be expressed in a complex spatial form as

$$\Phi(\mathbf{x};\,t)=\mathrm{Re}\left[\phi(\mathbf{x})\mathrm{e}^{-\mathrm{i}\omega t}\right], \tag{2}$$

where 'Re' stands for taking the real part; $\mathrm{i}=\sqrt{-1}$.

When considering the wave action with stationary bodies, the total velocity potential ϕ can be written as a summation of the incident potential ϕ_I and diffraction potential ϕ_D That is

$$\phi=\phi_I+\phi_D. \tag{3}$$

The incident velocity potential is due to the undisturbed dual-plane incident waves propagating at angles of β and $(\pi-\beta)$, respectively, and it is expressed as

$$\phi_I=-\frac{\mathrm{i}Ag}{\omega}\frac{\cosh\left[k(z+h)\right]}{\cosh(kh)}\mathrm{e}^{\mathrm{i}ky\sin\beta}\left(\mathrm{e}^{\mathrm{i}kx\cos\beta}+\mathrm{e}^{-\mathrm{i}kx\cos\beta}\right). \tag{4}$$

In Eq. (4), the wavenumber k is determined by dispersion relation $\omega^2=gk\tanh(kh)$ with g being the acceleration due to gravity.

Besides Laplace's equation, the velocity potentials are also required to satisfy proper conditions on the boundary surfaces. On the mean plane of the free surface $z = 0$, the combined kinematic and dynamic boundary condition is given by

$$\frac{\partial \phi}{\partial z} - \frac{\omega^2}{g}\phi = 0, \quad \text{on } z = 0. \tag{5}$$

On the mean wet surfaces of the real and imaginary vessels, which are denoted by S_b and S_b', respectively, the boundary condition is given by

$$\frac{\partial \phi}{\partial n} = 0, \quad \text{on } S_b \text{ and } S_b', \tag{6}$$

where $\mathbf{n} = (n_x, n_y, n_z)^T$ is the normal unit vector pointing outward from the fluid domain. In the same way, the boundary condition on the impermeable seabed ($z = -h$) is

$$\frac{\partial \phi}{\partial z} = 0, \quad \text{on } z = -h. \tag{7}$$

To ensure the uniqueness of the solution, ϕ_D has to satisfy the Sommerfeld radiation condition at a substantial distance from the structure. That is

$$\lim_{r\to\infty}\left[\sqrt{r}\left(\frac{\partial \phi_D}{\partial r} - \mathrm{i}k\phi_D\right)\right] = 0. \tag{8}$$

A boundary integral equation method is then used to solve the established boundary value problem. The oscillating source $G(\mathbf{x}, \mathbf{x}_0; \omega)$, which satisfies a linear free-surface boundary condition, a no-flow condition on the horizontal seabed, and a Sommerfeld radiation condition at infinity, is used as the Green's function. The use of Green's second identity to the velocity potential and the Green's function can lead to a Fredholm integral equation of the second kind for ϕ_D. Then, the resulting boundary-integral equation is expressed as follows

$$\alpha\phi_D(\mathbf{x}_0) - \iint_{S_b \cup S_b'} \frac{\partial G(\mathbf{x}, \mathbf{x}_0; \omega)}{\partial n}\phi_D(\mathbf{x})\,\mathrm{d}s = \iint_{S_b \cup S_b'} G(\mathbf{x}, \mathbf{x}_0; \omega)\frac{\partial \phi_I}{\partial n}\,\mathrm{d}s, \tag{9}$$

in which α is a measure of the normalized solid angle. α depends on the local shape of the boundary surface. The difficulty associated with the evaluation of α is overcome by formulating a complementary problem within the interior of the body surface with the application of an auxiliary Green's function.

A higher-order boundary element method (HOBEM) (Teng and Eatock Taylor, 1995) is then used to solve Eq. (9). S_b and S_b' are discretised into a number of 6-node quadratic triangular elements or 8-node quadratic quadrilateral elements for modelling both the geometry and the variation of potentials. The elements are then transformed into those in terms of isoparametric coordinates, and the integral within each element is evaluated using the node values. Then, we apply the collocation method, and a set of algebraic equations can be established. When the source point coincides with the field point, the difficulty associated with the singularity of Green's function is overcome with the aid of the polar coordinate transformation. In addition, singular integration of the derivative of Green's function would exist in the elements, including the source point. The summation of the integration in all the elements adjacent to the source point exists in the Cauchy principal value (CPV) sense. The direct method proposed in Teng et al. (2006) has been used to deal with the CPV integrals in this study. After solving the algebraic system, the potentials over the body surface are obtained.

3. Calculation of the free-surface elevation in the gap and induced wave forces

3.1 Calculation of the liner free-surface elevation and wave forces

After solving the wave diffraction problem and obtaining the velocity potential, the linear wave force on the vessel can be determined through the integration of the linear wave pressure over the body surface. That is

$$\mathbf{f} = \left(f_x, f_y, f_z\right)^T = \iint_{S_b} \left[\mathrm{i}\omega\rho\left(\phi_I + \phi_D\right)\mathbf{n}\right]\mathrm{d}s; \tag{10a}$$

$$\mathbf{m} = \left(m_x,\ m_y,\ m_z\right)^T = \iint_{S_b} \left[\mathrm{i}\omega\rho\left(\phi_I + \phi_D\right)\left(\hat{\mathbf{r}}\times\mathbf{n}\right)\right]\mathrm{d}s, \tag{10b}$$

where $\hat{\mathbf{r}} = \mathbf{x} - \mathbf{x}_o$ with $\mathbf{x}_o$ being the rotation centre. In this study, $\mathbf{x}_o$ is at the centre of the vessel on the free surface, i.e., $(-(e + b/2), 0, 0)$.

The free-surface elevation amplitude, denoted by η hereinafter, can be expressed as

$$\eta\left(x_0, y_0\right) = \frac{\mathrm{i}\omega}{g}\left[\phi_I\left(\mathbf{x}_0\right) + \phi_D\left(\mathbf{x}_0\right)\right]\Big|_{z_0=0}. \tag{11}$$

In Eq. (11), the diffraction potential is determined according to Eq. (9) with z_0 located on the free surface.

To capture the rapid variation of the free surface in the narrow gap, refined meshes are required. $\mathbf{x}_0$ can be very close to the vessel's surface in some conditions, leading to a nearly singular integration. To overcome the difficulty associated with the troublesome integration, a self-adaptive Gauss integration method is applied. When the integration over a certain element turns out to be nearly singular, this element will be divided into sub-elements. Such subdivisions will continue until the distance between the source and the field points is greater than the characteristic size of each sub-element. As a result, the original integration in an element is transformed into a series of sub-integrations over finer sub-elements with more Gauss points.

3.2 Calculation of the mean wave drift force based on the direct pressure integration

Besides the first-order wave force, the second-order mean wave drift force can also be calculated based on the linear wave theory. It is generally understood that the second-order difference-frequency wave force is the main excitation of the slow-drift motion. Reliable numerical and semi-analytical solutions for the second-order wave force in bi-chromatic waves have been developed by researchers such as Kim and Yue (1990), Eatock Taylor and Huang (1997), Teng and Cong (2017), Cong et al. (2018), Heo and Kashiwagi (2020) and Shao et al. (2022). When the frequency difference is small, Newman (1974) expanded the complete difference-frequency wave force into Taylor's series with respect to the frequency difference, and only the zero-order component is retained. Consequently, the exact difference-frequency wave force is approximated by the mean force on structures in regular waves. Newman's approximation shows that the mean wave drift force can play an important role in the low-frequency behaviour of a floating body.

The mean wave drift force can be calculated in a straightforward manner based on the direct pressure integration of the quadratic pressure over the vessel surface, namely the near-field formulation. The near-field formulation has been derived in some

previous studies, such as Ogilvie (1983). Then, the mean wave drift force and moment on the vessel, denoted by $\mathbf{f}^-$ and $\mathbf{m}^-$ hereinafter, can be determined according to:

$$\mathbf{f}^- = -\frac{\rho}{4}\iint_{S_b}\left(\nabla\phi\cdot\nabla\phi^*\mathbf{n}\right)\mathrm{d}s + \frac{\rho g}{4}\oint_{\Gamma_b}\left(\eta\eta^*\mathbf{n}'\right)\mathrm{d}l; \tag{12}$$

$$\mathbf{m}^- = -\frac{\rho}{4}\iint_{S_b}\left[\nabla\phi\cdot\nabla\phi^*\left(\hat{\mathbf{r}}\times\mathbf{n}\right)\right]\mathrm{d}s + \frac{\rho g}{4}\oint_{\Gamma_b}\left[\eta\eta^*\left(\hat{\mathbf{r}}\times\mathbf{n}'\right)\right]\mathrm{d}l, \tag{13}$$

where subscript * represents the complex conjugate; Γ_b is the intersection of S_b with $z = 0$; $\mathbf{n}' = \mathbf{n}\Big/\sqrt{1-n_z^2}$.

After dividing S_b into a series of quadratic elements and defining the shape function over each element, the velocity potential and its spatial derivatives can be obtained at the integration points by means of the shape function. Then, the integrals in Eqs. (12) and (13) can be evaluated numerically based on the Gauss-Legendre quadrature rule.

3.3 Calculation of the mean wave drift force using a semi-cylindrical control surface

3.3.1 Derivation of the formulation involving a semi-cylindrical control surface

Besides the near-field formulation, the computation can also be achieved by using the far-field formulation or applying the technique of control surfaces (Chen, 2007; lee, 2007; Liang and Chen, 2017). For a multi-body system, the conventional far-field formulation is restricted to give the global force on the system. In the meantime, the method involving control surfaces takes the obvious advantage that it can give the wave force on each individual body of a multi-body system. In view of this, the technique of control surfaces in conjunction with HOBEM has been used to calculate the mean wave force on a vessel alongside a vertical wall.

A fictitious semi-cylinder enclosing the vessel is then considered. It is defined by $0 \le r \le R_c$, $\pi/2 \le \theta \le 3\pi/2$, and $-h \le z \le \zeta$. The boundary surfaces of the semi-cylinder are S_C, $\hat{S}_W$, $\hat{S}_F$, and $\hat{S}_d$, respectively. S_C represents a semi-cylindrical control surface, extending from the seabed to the free surface. $\hat{S}_W$, $\hat{S}_F$, and $\hat{S}_d$ are the intersection

of the semi cylinder with the free surface, the seabed and the vertical wall, respectively. In the control volume limited by S_B, S_C, $\hat{S}_W$, $\hat{S}_F$, and $\hat{S}_d$, the linear momentum can be expressed as

$$\frac{\mathrm{d}}{\mathrm{d}t}\begin{Bmatrix}\mathbb{M}_x\\ \mathbb{M}_y\end{Bmatrix} = -\iint_{S_C\cup S_B\cup\hat{S}_W\cup\hat{S}_F\cup\hat{S}_d}\left[P\begin{Bmatrix}n_x\\ n_y\end{Bmatrix}+\rho\begin{Bmatrix}u\\ v\end{Bmatrix}(\mathbf{u}\cdot\mathbf{n}-U_n)\right]\mathrm{d}s, \tag{14}$$

where P is the pressure exerted by the fluid; U_n is the normal velocity of the boundary surface; $\mathbf{u} = (u, v, w)^T$ is the vector of fluid velocity. On $\hat{S}_F$, it is required that $\mathbf{u}\cdot\mathbf{n} - U_n = 0$. On S_B, $\hat{S}_W$, and $\hat{S}_d$, it is required that $\mathbf{u}\cdot\mathbf{n} = 0$ and $U_n = 0$. The control surface S_C is fixed, yielding $U_n = 0$ on S_C. The fluid pressure over the free surface is equivalent to the atmospheric pressure, which is assumed zero. In addition, within the framework of potential flow theory, fluid velocity can be expressed as the derivative of velocity potential. Then, we can relate the wave force on the vessel to the changing rate of the linear momentum in the control volume. That is

$$\begin{Bmatrix}F_x\\ F_y\end{Bmatrix} = \iint_{S_B} P\begin{Bmatrix}n_x\\ n_y\end{Bmatrix}\mathrm{d}s = -\iint_{S_C}\left[P\begin{Bmatrix}n_x\\ n_y\end{Bmatrix}+\rho\begin{Bmatrix}u\\ v\end{Bmatrix}\mathbf{u}\cdot\mathbf{n}\right]\mathrm{d}s - \iint_{\hat{S}_W} P\begin{Bmatrix}n_x\\ n_y\end{Bmatrix}\mathrm{d}s - \frac{\mathrm{d}}{\mathrm{d}t}\begin{Bmatrix}\mathbb{M}_x\\ \mathbb{M}_y\end{Bmatrix}. \tag{15}$$

When the time average is taken, and the periodicity is invoked, the last term on the right-hand side of Eq. (15) gives no contribution. Then, the second-order mean wave drift force on the vessel is expressed as

$$\begin{Bmatrix}\bar{f}_x\\ \bar{f}_y\end{Bmatrix} = -\overline{\left\{\iint_{S_C}\left[P\begin{Bmatrix}n_x\\ n_y\end{Bmatrix}+\rho\begin{Bmatrix}u\\ v\end{Bmatrix}\mathbf{u}\cdot\mathbf{n}\right]\mathrm{d}s + \iint_{\hat{S}_W} P\begin{Bmatrix}n_x\\ n_y\end{Bmatrix}\mathrm{d}s\right\}}, \tag{16}$$

where the overbar indicates the mean value in a wave period.

Analogous to the analysis of wave force, we can relate the wave moment on the vessel to the changing rate of the angular momentum in the control volume. Then, the following expression can be obtained for mean wave drift moment $\bar{m}_z$ with respect to the rotation centre:

$$\bar{m}_z = -\mathbf{k}\cdot\overline{\left\{\iint_{S_C\cup\hat{S}_W}\left[P(\hat{\mathbf{r}}\times\mathbf{n})\right]\mathrm{d}s - \iint_{S_C}\left[\rho(\mathbf{n}\cdot\mathbf{u})(\hat{\mathbf{r}}\times\mathbf{u})\right]\mathrm{d}s\right\}}. \tag{17}$$

For the harmonic incident waves, after using Bernoulli's equation and Taylor's series expansion, Eqs. (16) and (17) can be further expressed as

$$f_x^- = \frac{\rho}{4}\mathrm{Re}\left\{\iint_{S_c}\left[\left(\nabla\phi\cdot\nabla\phi^*\right)n_x - 2\frac{\partial\phi}{\partial x}\frac{\partial\phi^*}{\partial n}\right]\mathrm{d}s - g\oint_{\Gamma_c}\left(\eta\eta^* n_x\right)\mathrm{d}l + \iint_{\hat{S}_w}\left[\left(\nabla\phi\cdot\nabla\phi^*\right)n_x\right]\mathrm{d}s - g\oint_{\hat{\Gamma}_w}\left(\eta\eta^* n_x\right)\mathrm{d}l\right\}; \tag{18a}$$

$$f_y^- = \frac{\rho}{4}\mathrm{Re}\left\{\iint_{S_c}\left[\left(\nabla\phi\cdot\nabla\phi^*\right)n_y - 2\frac{\partial\phi}{\partial y}\frac{\partial\phi^*}{\partial n}\right]\mathrm{d}s - g\int_{\Gamma_c}\left(\eta\eta^* n_y\right)\mathrm{d}l\right\}; \tag{18b}$$

$$m_z^- = \frac{\rho}{4}\mathbf{k}\cdot\mathrm{Re}\left\{\iint_{S_c}\left[\left(\nabla\phi\cdot\nabla\phi^*\right)(\hat{\mathbf{r}}\times\mathbf{n}) - 2\frac{\partial\phi}{\partial n}\left(\hat{\mathbf{r}}\times\nabla\phi^*\right)\right]\mathrm{d}s - g\oint_{\Gamma_c}\left[\left(\eta\eta^*\right)(\hat{\mathbf{r}}\times\mathbf{n})\right]\mathrm{d}l + \iint_{\hat{S}_w}\left[\left(\nabla\phi\cdot\nabla\phi^*\right)(\hat{\mathbf{r}}\times\mathbf{n})\right]\mathrm{d}s - g\oint_{\hat{\Gamma}_w}\left[\left(\eta\eta^*\right)(\hat{\mathbf{r}}\times\mathbf{n})\right]\mathrm{d}l\right\}, \tag{18c}$$

where S_c is the mean control surface, and defined by $r = R_c$, $-h \le z \le 0$, and $\pi/2 \le \theta \le 3\pi/2$; $\hat{S}_w$ is defined by $x = 0$, $-R_c \le y \le R_c$, and $-h \le z \le 0$; Γ_c and $\hat{\Gamma}_w$ are the intersection of S_c and $\hat{S}_w$ with $z = 0$, respectively. The normal vector on S_c is defined as positive when pointing to the far-field region. In addition, the normal vector on $\hat{S}_w$ points to the positive x direction.

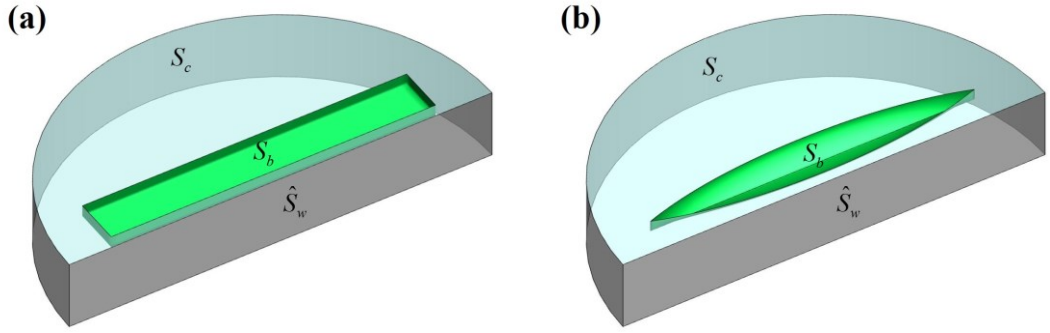

Fig. 3 Definition of the semi-cylindrical control surface surrounding (a) a rectangular barge and (b) a Wigley hull

3.3.2 Numerical evaluation of the mean wave drift force based on the derived formulation

Compared with Eq. (13) which is based on the direct pressure integration, the new expressions of the mean wave drift force and moment in Eq. (18) no longer involve the quantities over the body surface. However, the velocity potential and its derivative over S_c and $\hat{S}_w$ are required.

The use of a semi-cylindrical control surface takes the obvious advantage that the velocity potential and its derivative over the control surface can be calculated in an analytical way. Fig. 3 shows the definition of the semi-cylindrical control surface surrounding a rectangular barge and a Wigley hull, respectively. Over S_c, which is smooth and at a distance from the vessel, the velocity potential can be expressed into a Fourier series of polar angle θ, where $\theta=\tan^{-1}(y/x)$. Then, we can present Green's function S_c in the form of a discrete eigenfunction expansion using Graf's addition theorem:

$$G(\mathbf{x},\ \mathbf{x}_0;\ \omega)=\sum_{m=-\infty}^{+\infty}\left[G(r_0,\ \theta_0,\ z_0;\ r,\ z)e^{-\mathrm{i}m\theta}\right], \tag{19}$$

where

$$\begin{aligned}G_m(r_0,\ \theta_0,\ z_0;\ r,\ z)=&-\frac{\mathrm{i}}{2}\left\{\frac{2k\cosh\left[k(z_0+h)\right]\cosh\left[k(z+h)\right]H_m(kr_>)J_m(kr_<)}{\sinh(2kh)+2kh}\right\}e^{\mathrm{i}m\theta_0}\\&-\frac{1}{\pi}\sum_{n=1}^{\infty}\left\{\frac{2k_n\cos\left[k_n(z_0+h)\right]\cos\left[k_n(z+h)\right]K_m(k_nr_>)I_m(k_nr_<)}{\sin(2k_nh)+2k_nh}\right\}e^{\mathrm{i}m\theta_0},\end{aligned} \tag{20}$$

with $\theta_0=\tan^{-1}(y_0/x_0)$; $r=\sqrt{x^2+y^2}$; $r_0=\sqrt{x_0^2+y_0^2}$. In Eq. (20), $r_>=\max(r_0, r)$; $r_<=\min(r_0, r)$; k_n is the nth positive real root of $\omega^2=-gk_n\tan(k_nh)$; H_m is the Hankel function of the first kind of order m; I_m and K_m are the modified Bessel functions of the first and second kind of order m, respectively. Based on Graf's addition theorem, the incident velocity potential can be expressed in the cylindrical coordinate as:

$$\phi_I(\mathbf{x}_0)=\sum_{m=-\infty}^{+\infty}\left[T_m(r_0,\ z_0)e^{\mathrm{i}m\theta}\right], \tag{21}$$

where

$$T(r_0,\ z_0)=-\frac{\mathrm{i}Ag}{\omega}\frac{\cosh\left[k(z_0+h)\right]}{\cosh(kh)}\left[e^{-\mathrm{i}m\beta}+e^{-\mathrm{i}m(\pi-\beta)}\right]\mathrm{i}^mJ_m(kr_0). \tag{22}$$

Based on Eqs. (19) to (22) and applying Green's second identity, the diffraction velocity potential can be expressed in the following form:

$$\phi_D(\mathbf{x}_0)=\sum_{m=-\infty}^{+\infty}\left[D_m(r_0,\ z_0)e^{\mathrm{i}m\theta_0}\right], \tag{23}$$

where

$$D_m(r_0,\ z_0)=-\frac{\mathrm{i}}{2}\frac{2k\cosh\left[k(z_0+h)\right]}{\sinh(2kh)+2kh}H_m(kr_0)B_{m,\,0}-\frac{1}{\pi}\sum_{n=1}^{+\infty}\left\{\frac{2k_n\cos\left[k_n(z_0+h)\right]}{\sin(2k_nh)+2k_nh}K_m(k_nr_0)B_{m,\,n}\right\}, \tag{24}$$

with

$$B_{m,\,0}=\iint_{S_b}\left\{\left(\phi_D\frac{\partial}{\partial n}+\frac{\partial\phi_I}{\partial n}\right)J_m\left(kr\right)\cosh\left[k\left(z+h\right)\right]e^{-\mathrm{i}m\theta}\right\}\mathrm{d}s; \tag{25a}$$

$$B_{m,\,n}=\iint_{S_b}\left\{\left(\phi_D\frac{\partial}{\partial n}+\frac{\partial\phi_I}{\partial n}\right)I_m\left(k_nr\right)\cos\left[k_n\left(z+h\right)\right]e^{-\mathrm{i}m\theta}\right\}\mathrm{d}s. \tag{25b}$$

Then, when $\mathbf{x}_0$ is on the control surface S_c, we can obtain that

$$\phi\left(\mathbf{x}_0\right)=\sum_{m=-\infty}^{+\infty}\left[T_m\left(r_0,\,z_0\right)+D_m\left(r_0,\,z_0\right)\right]e^{\mathrm{i}m\theta_0}, \tag{26}$$

and

$$\left.\frac{\partial\phi}{\partial r}\right|_{\mathbf{x}=\mathbf{x}_0}=\sum_{m=-\infty}^{+\infty}\left\{\left[\frac{\partial T_m\left(r,\,z\right)}{\partial r}+\frac{\partial D_m\left(r,\,z\right)}{\partial r}\right]e^{\mathrm{i}m\theta}\right\}\Bigg|_{\mathbf{x}=\mathbf{x}_0}; \tag{27a}$$

$$\left.\frac{\partial\phi}{\partial\theta}\right|_{\mathbf{x}=\mathbf{x}_0}=\sum_{m=-\infty}^{+\infty}\left\{\mathrm{i}m\left[T_m\left(r,\,z\right)+D_m\left(r,\,z\right)\right]e^{\mathrm{i}m\theta}\right\}\Big|_{\mathbf{x}=\mathbf{x}_0}; \tag{27b}$$

$$\left.\frac{\partial\phi}{\partial z}\right|_{\mathbf{x}=\mathbf{x}_0}=\sum_{m=-\infty}^{+\infty}\left\{\left[\frac{\partial T_m\left(r,\,z\right)}{\partial z}+\frac{\partial D_m\left(r,\,z\right)}{\partial z}\right]e^{\mathrm{i}m\theta}\right\}\Bigg|_{\mathbf{x}=\mathbf{x}_0}. \tag{27c}$$

We then consider the case when $\mathbf{x}_0$ is located on $\hat{S}_w$. The following integral equation method is used to determine the velocity potential:

$$\phi\left(\mathbf{x}_0\right)=\iint_{S_b\cup S_b'}\left[\frac{\partial G\left(\mathbf{x},\,\mathbf{x}_0;\,\omega\right)}{\partial n}\phi_D\left(\mathbf{x}\right)+G\left(\mathbf{x},\,\mathbf{x}_0;\,\omega\right)\frac{\partial\phi_I\left(\mathbf{x}\right)}{\partial n}\right]\mathrm{d}s+\phi_I\left(\mathbf{x}_0\right). \tag{28}$$

As a no flow is held on $x = 0$, the derivative of the velocity potential with respect to x is zero on $\hat{S}_w$. In addition, the derivatives with respect to y and z are evaluated numerically with the aid of shape functions.

After obtaining the velocity potential and its derivatives over S_c and $\hat{S}_w$, the mean wave drift force can be evaluated based on Eq. (18) by the application of the Gauss-Legendre quadrature rule with S_c and $\hat{S}_w$ being divided into a series of quadratic elements.

4. Convergence test and validation

To verify the reliability of the developed model, the convergence of the results with respect to the mesh discretization is then examined. A rectangular barge as well as a Wigley hull, which are both of length l = 276 m, width b = 46 m and draft d = 13.8 m,

are firstly taken as examples. The vessel is placed in front of a vertical wall at a constant water depth h = 92 m. The gap width between the vessel and the vertical wall is e = 4.6 m. Computation is then conducted for the mean wave drift force in the horizontal plane and the mean yaw moment. Prior to that, meshing is simplified by discretising the first quadrant of the body surface due to the geometrical symmetry. Two discretisation strategies, namely Mesh 1 and Mesh 2, are employed in the test. In Mesh 1, 588 and 448 quadrilateral elements are used in a quadrant of the rectangular barge and the Wigley hull, respectively. Whereas the number of elements in Mesh 2 increases to 900 and 780, respectively, as depicted in Fig. 4. Numerical computation is then conducted based on the near-field formulation. Even though Mesh 1 is much coarser than Mesh 2, they lead to almost the same results as shown in Figs. 5-6, indicating that convergence is achieved. In addition, for the purpose of validation, the calculation by applying a semi-cylindrical control surface has also been conducted, and the results have been added in Figs. 5-6. In the computation, the mesh discretization over the body surface follows the scheme Mesh 2, and S_c and $\hat{S}_w$ are divided into a total of 1035 quadrilateral elements with R_c = 250 m. As shown in Figs. 5-6, the results based on different formulations are in good agreement.

We then consider the test case of wave interaction with a bottom-mounted surface-piecing vertical column in front of a vertical wall. The radius of the column is a, the water depth d equals $5a$, and the distance between the centre of the column and the vertical wall equals $2a$ in the horizontal plane. Semi-analytical solutions to the mean wave drift force on a column array in front of a long vertical wall have been developed by Cong et al. (2020), which provides a useful benchmark for the present computation. In the present computation, 104 quadrilateral elements over the body surface are used in a quadrant, and S_c and $\hat{S}_w$ are divided into a total of 500 quadrilateral elements with $R_c = 5a$. In Figs. 7-8, an excellent agreement is achieved between present results and semi-analytical results, further confirming the validity of the present solution.

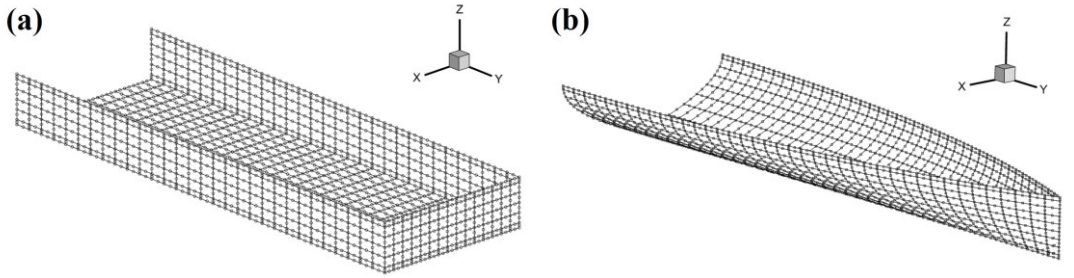

Fig. 4. Computational meshes in a quadrant area for the cases of (a) a rectangular barge and (b) a Wigley hull in front of a vertical wall with the discretisation strategy Mesh 2.

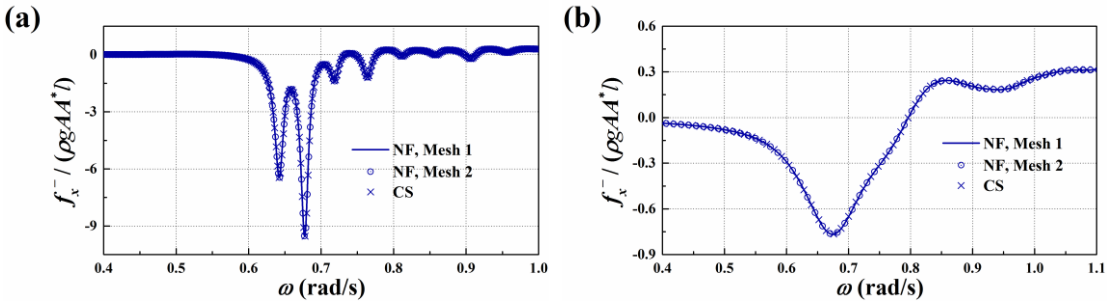

Fig. 5. Comparison of the horizontal mean wave drift force on (a) a rectangular barge and (b) a Wigley hull in front of a vertical wall based on different methods with $e = 4.6$ m and $\beta = 30°$. 'NF' denotes the results based on the near-field formulation; 'CS' denotes those by using the control surface.

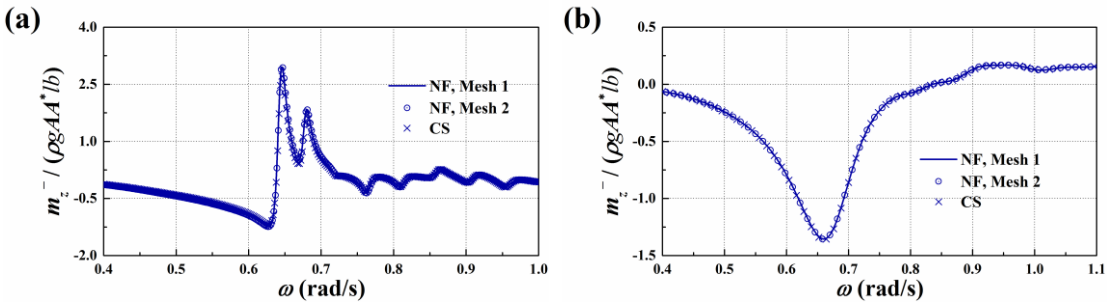

Fig. 6. Comparison of the mean yaw moment on (a) a rectangular barge and (b) a Wigley hull in front of a vertical wall based on different methods with $e = 4.6$ m and $\beta = 30°$

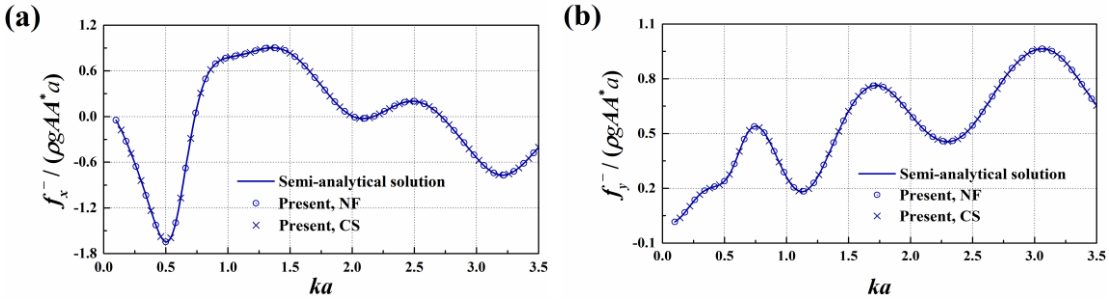

Fig. 7. Comparison of the mean wave drift force on a vertical column in front of a vertical wall with $\beta = 30°$.

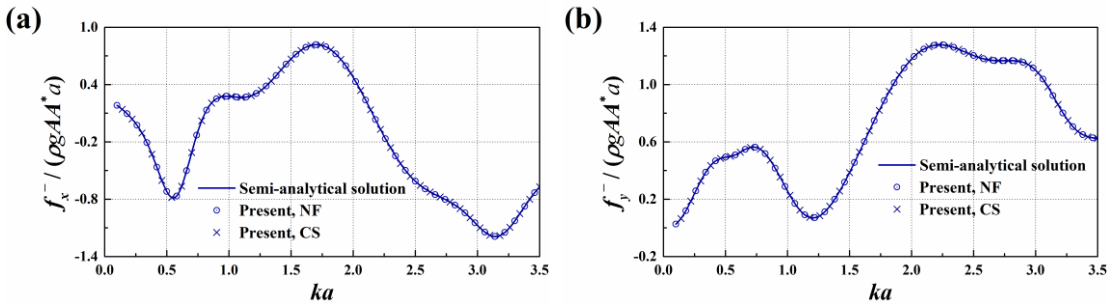

Fig. 8. Comparison of the mean wave drift force on a vertical column in front of a vertical wall with $\beta = 45°$.

5. Numerical results and discussion

Detailed numeral studies are conducted in this section for both normal and oblique sea conditions. The dimensions of the vessel are the same as those in the convergence test, i.e., $l = 276$ m, $b = 46$ m and $d = 13.8$ m. The water depth is $h = 92.0$ m. In addition, four points on the free surface in the gap, namely P_1, P_2, P_3 and P_4, are introduced as featured points. The coordinates of P_1 to P_4 in the horizontal plane are ($-e/2$, –0.0 m), ($-e/2$, –60.0 m), ($-e/2$, –90.0 m) and ($-e/2$, –120.0 m), respectively.

5.1 Free-surface elevation

We then consider the case of a berthed rectangular barge. The variation of the linear free-surface elevation amplitude at P_1 to P_4 with respect to the wave frequency is shown in Figs. 9, 10 and 11. In the calculation, the wave heading is varied as $\beta = 0°$, 15° and 30°, and the spacing between the long wall and the barge is $e = 4.6$ m. The free-surface elevation amplitude is characterized by a series of apparent peaks. The peaks corresponding to different wave headings are not at identical frequencies. Under oblique incidence, the propagating waves along the gap get more significant. They can superimpose on the nearly standing wave field when resonance occurs and then cause a shift in the peak frequencies. The resulting shift is more apparent at the lower frequencies.

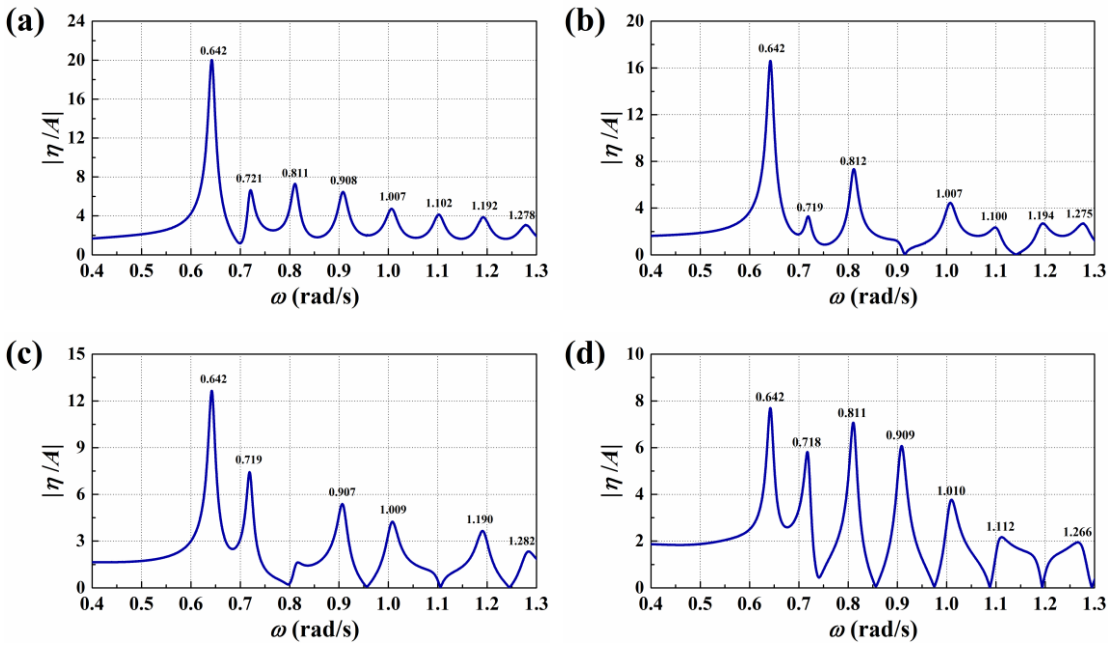

Fig. 9. Variation of the free-surface elevation amplitude at the featured points P_1 to P_4 with $e = 4.6$ m and $\beta = 0°$ for the case of a rectangular barge: (a) P_1, (b) P_2, (c) P_3, and (d) P_4

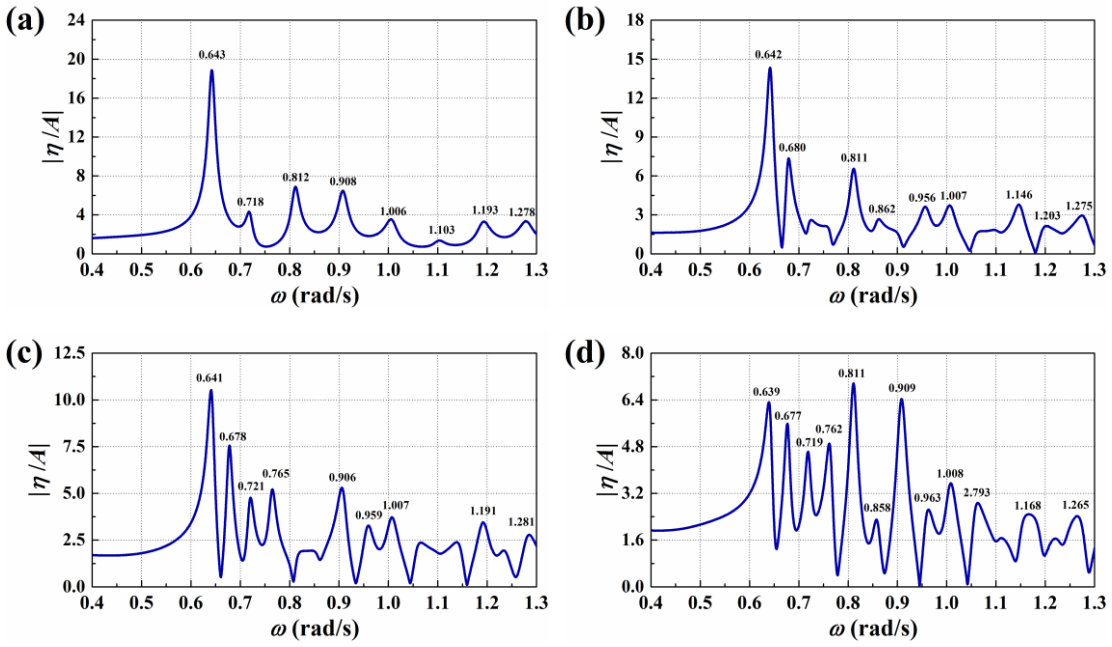

Fig. 10. Variation of the free-surface elevation amplitude at the featured points P_1 to P_4 with $e = 4.6$ m and $\beta = 15°$ for the case of a rectangular barge: (a) P_1, (b) P_2, (c) P_3, and (d) P_4

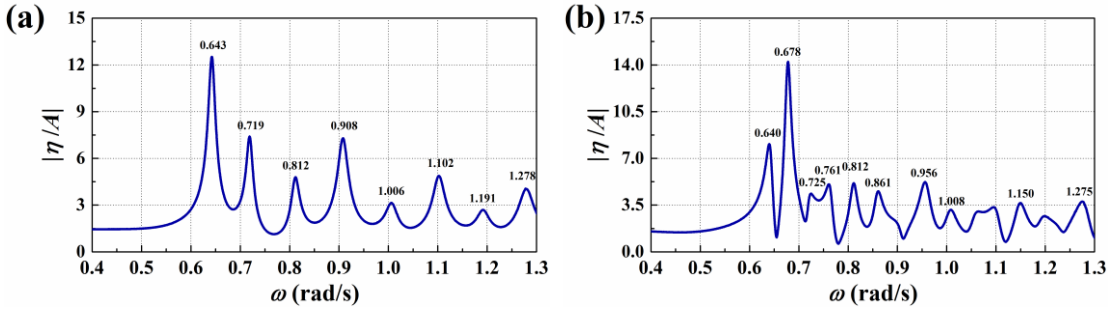

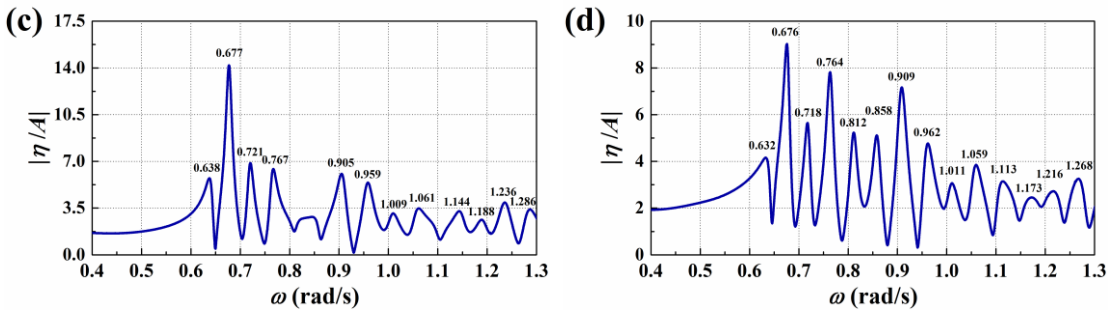

Fig. 11. Variation of the free-surface elevation amplitude at the featured point P_1 to P_4 with e = 4.6 m and β = 30° for the case of a rectangular barge: (a) P_1, (b) P_2, (c) P_3, and (d) P_4

Analogous results to those in Fig. 11 but with the spacing e = 9.2 m are shown in Fig. 12. The comparison of the results with e = 4.6 m and 9.2 m shows that the frequencies of the apparent peaks depend on the spacing, and the magnitudes of the peaks decrease with increasing spacing.

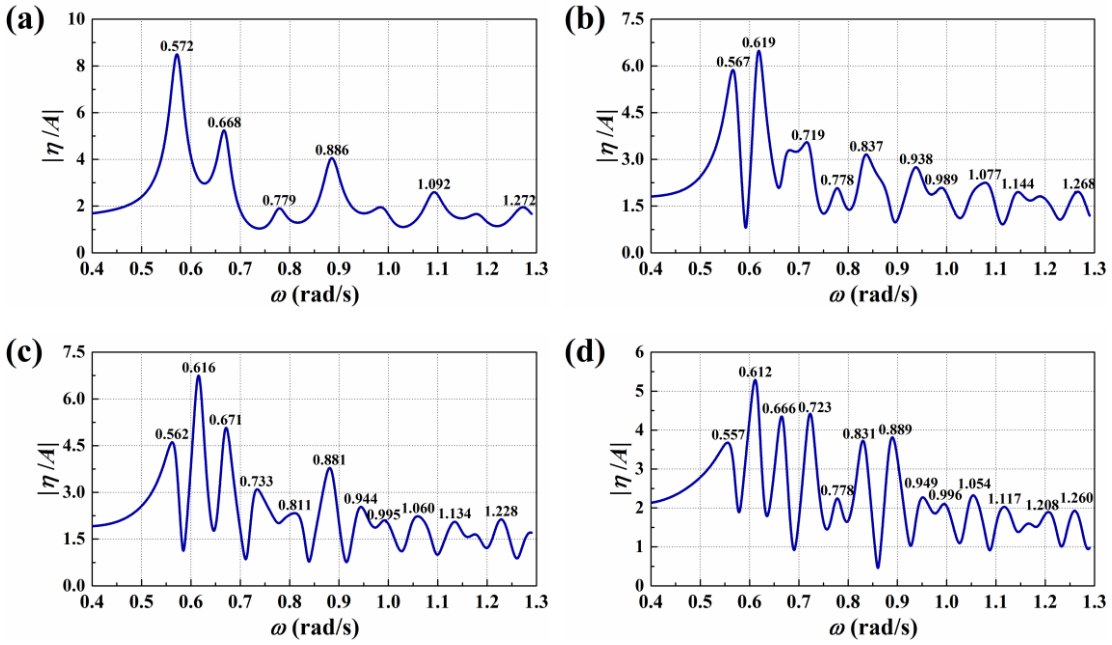

Fig. 12. Variation of the free-surface elevation amplitude at the featured points P_1 to P_4 with e = 9.2 m and β = 30° for the case of a rectangular barge: (a) P_1, (b) P_2, (c) P_3, and (d) P_4

The prediction of moonpool resonant frequencies, which has been comprehensively investigated by Molin (2001), can be used to inform the understanding of gap resonance. However, the boundary condition at the gap ends differs from that for the moonpool. In Sun et al. (2010), an analytical model was developed to predict the resonant frequencies for the three-dimensional flow. This model is similar to that for the moonpool but

assumes an open (zero pressure) condition at the gap ends. We denote mode (m, n) corresponds to a scattered mode having m and n half wavelengths along the length and width direction, respectively. Then, following Sun et al. (2010), the resonant frequency for mode (m, n), which is denoted by ω_{mn} hereinafter, can be determined according to

$$\omega_{mn}^2 = g\nu_{mn}\frac{1+J_{mn}\tanh(\nu_{mn}h)}{J_{mn}+\tanh(\nu_{mn}h)}, \tag{29}$$

where

$$J_{mn} = \frac{\nu_{mn}}{2\pi}\frac{\int_0^l\int_0^l\int_0^b\int_0^b\left[\frac{1}{R}f_m(\xi)\cdot f_m(\xi')\cdot g_n(\eta)\cdot g_n(\eta')\right]\mathrm{d}\xi\mathrm{d}\xi'\mathrm{d}\eta\mathrm{d}\eta'}{\int_0^l\int_0^b\left[f_m(\xi)\cdot f_m(\xi)\cdot g_n(\eta)\cdot g_n(\eta)\right]\mathrm{d}\xi\mathrm{d}\eta}. \tag{30}$$

In Eqs. (29) and (30), $f_m(\xi)=\sin(\lambda_m\xi)$; $g_n(\eta)=\cos(\mu_n\eta)$; $R=\sqrt{(\xi-\xi')^2+(\eta-\eta')^2}$; $\lambda=m\pi/l$; $\mu_n=n\pi/b$. When the gap is narrow, the free-surface motion along the gap width is dominated by the piston motion mode ($n=0$). Based on the method by Molin (2001) the quadruple integral in Eq. (30) can be reduced to a single integral by using the residue theorem in the case of $n=0$.

Table 1. Comparison of the resonant frequencies ω_{mn} for the free-surface elevation in the gap between a rectangular barge and a vertical wall with l = 276 m and b = 46 m. The results on the first line are based on the analytical method; the results on the second line are based on the numerical analysis of the free-surface elevation at P_4 when β = 30°.

e = \ (m, n) =	(1, 0)	(2, 0)	(3, 0)	(4, 0)	(5, 0)	(6, 0)	(7, 0)	(8, 0)	(9, 0)	(10, 0)
4.6 m	0.610	0.668	0.717	0.767	0.817	0.868	0.919	0.970	1.020	1.069
	0.632	0.676	0.718	0.764	0.812	0.858	0.909	0.962	1.011	1.059
9.2 m	0.531	0.606	0.669	0.730	0.789	0.847	0.904	0.959	1.012	1.063
	0.557	0.612	0.666	0.723	0.778	0.831	0.889	0.949	0.996	1.054

The comparison of the peak frequencies from the numerical analysis with those from the analytical model is shown in Table 1. A close agreement can be seen from Table 1. The discrepancy can be attributed to that the zero pressure boundary conditions at the gap ends have been used in the analytical model. The comparison shown in Table 1 indicates that the apparent peaks of the free-surface elevation at P_1 to P_4 are caused by the resonant fluid motion within the gap.

The distribution of the free-surface elevation amplitude corresponding to different resonant modes is shown in Figs. 13 and 14 for $\beta = 0°$ and 30°, respectively. It is made clear from these figures that the mode shapes are characterised by the evident odd and even peaks within the gap. Due to the symmetry of the barge-wall system, in beam seas ($\beta = 0°$), only the odd modes can be induced (see Fig. 13). In the meantime, the oblique wave action ($\beta = 30°$) can motivate both the odd and even modes of fluid motion (see Fig. 14). The free-surface elevation amplitude and its phase along $x = -e/2$ are depicted in Figs. 15 and 16. The mode (m, 0) corresponds to a scattered mode having m half wavelengths along the gap length. Correspondingly, the overall gap can be divided into a number of m sub-regions, and the fluid motion within the neighbouring sub-regions is almost out of phase. When a peak is attained within a certain sub-region, troughs are attained at the same time within the neighboring sub-regions, which in turn forms the nearly standing wave motion.

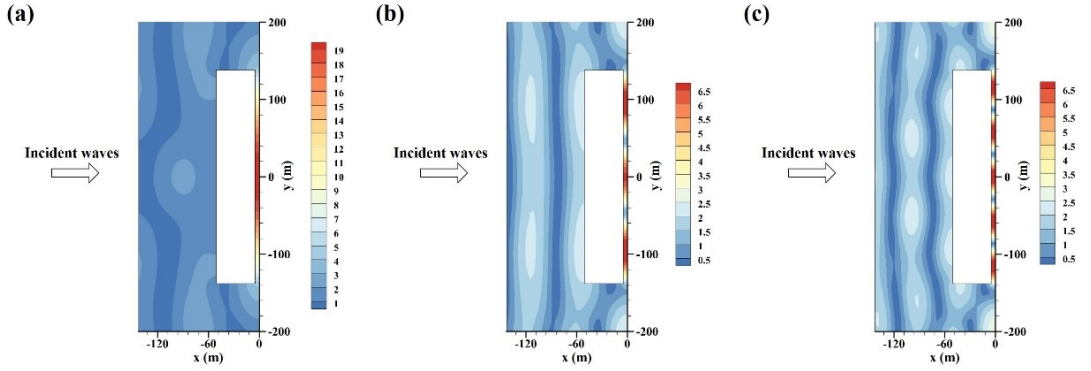

Fig. 13. Distribution of the free-surface elevation amplitude in the vicinity of a rectangular barge in front of a vertical wall when $\beta = 0°$ for (a) $\omega = 0.642$ rad/s, (b) $\omega = 0.721$ rad/s, and (c) $\omega = 0.811$ rad/s

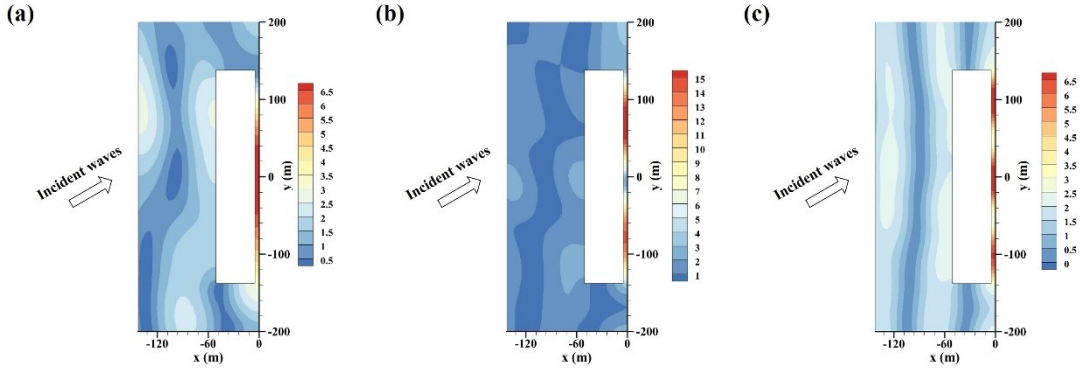

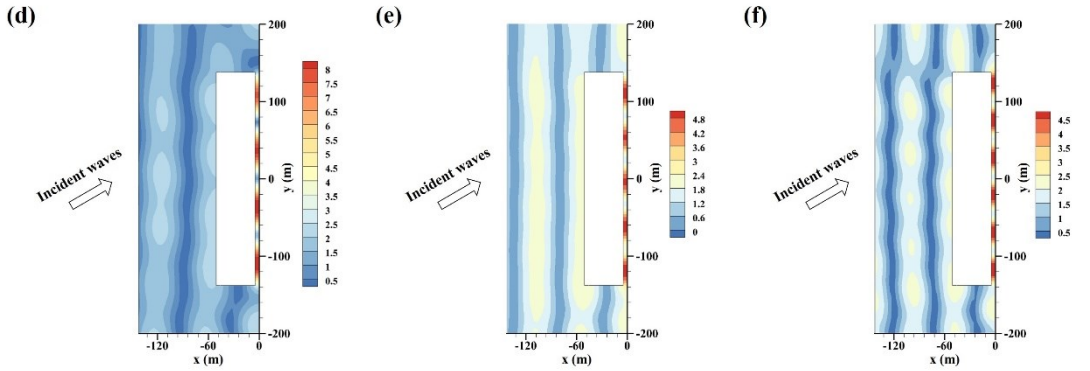

Fig. 14. Distribution of the free-surface elevation amplitude in the vicinity of a rectangular barge in front of a vertical wall when $\beta = 30°$ for (a) $\omega = 0.632$ rad/s, (b) $\omega = 0.676$ rad/s, (c) $\omega = 0.718$ rad/s, (d) $\omega = 0.764$ rad/s, (e) $\omega = 0.812$ rad/s, and (f) $\omega = 0.858$ rad/s.

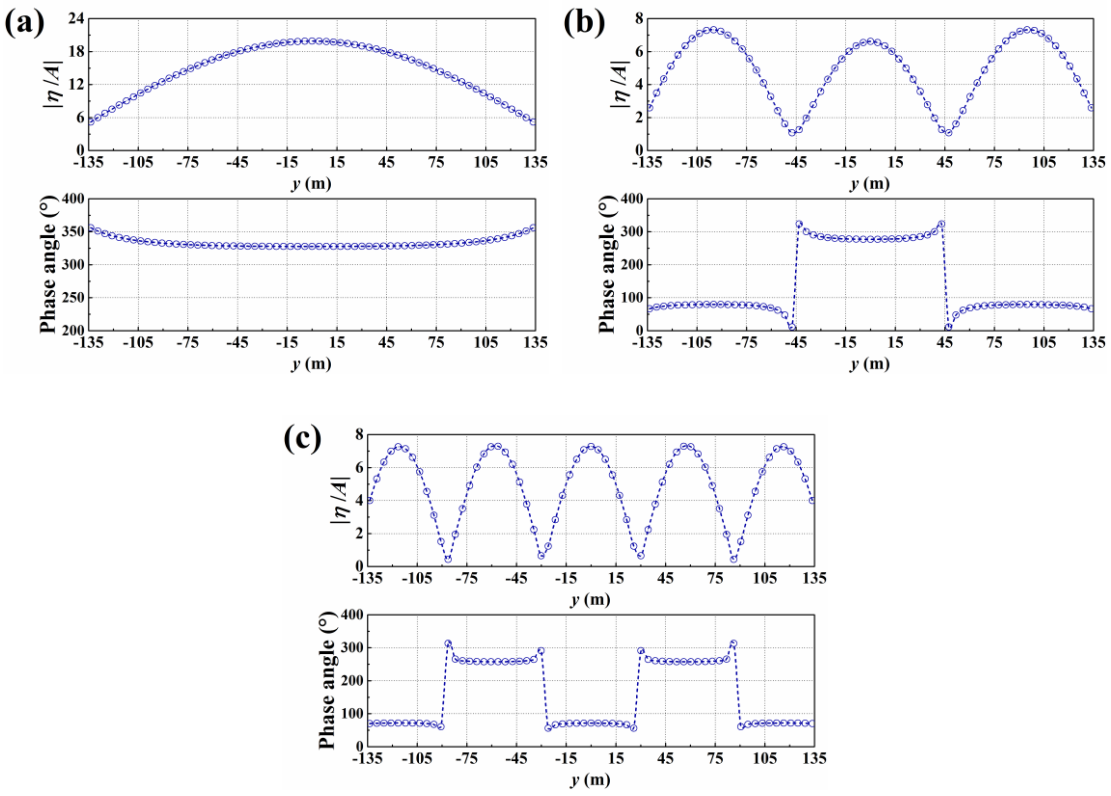

Fig. 15. Variation of the free-surface elevation amplitude and its phase along $x = -e/2$ when $\beta = 0°$ for the case of a rectangular barge: (a) $\omega = 0.642$ rad/s, (b) $\omega = 0.721$ rad/s, and (c) $\omega = 0.811$ rad/s.

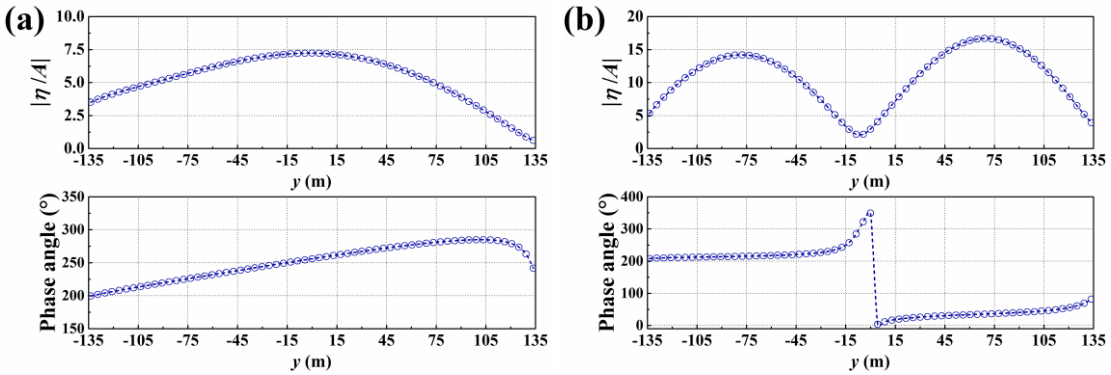

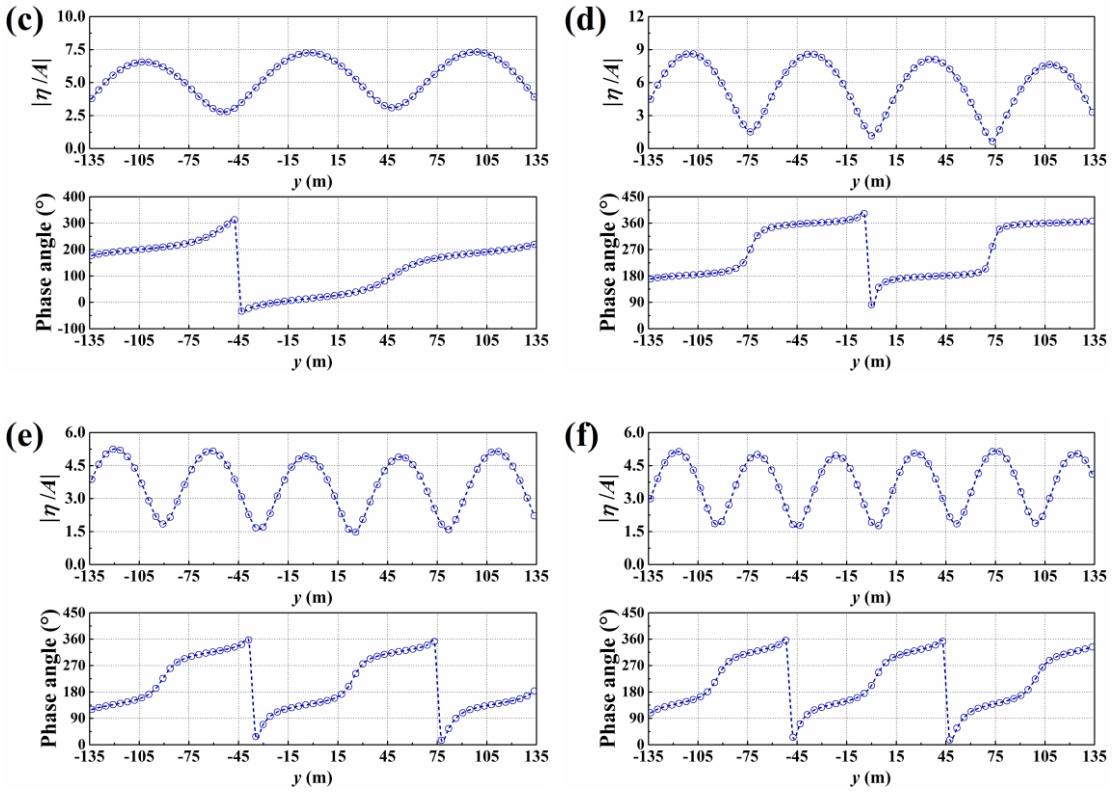

Fig. 16. Variation of the free-surface elevation amplitude and its phase along $x = -e/2$ when $\beta = 30°$ for the case of a rectangular barge: (a) $\omega = 0.632$ rad/s, (b) $\omega = 0.676$ rad/s, (c) $\omega = 0.718$ rad/s, (d) $\omega = 0.764$ rad/s, (e) $\omega = 0.812$ rad/s, and (f) $\omega = 0.858$ rad/s.

The variation of the free-surface elevation amplitude at the gap centre (0, 0) is shown in Fig. 17 for different gap lengths, i.e., $l = 2b$, $3b$, $4b$ and $+\infty$. $l = +\infty$ corresponds to a limiting case that the barge length tends to infinity. Then, the barge-wall system can be regarded as a two-dimensional one. A semi-analytical solution has been developed for a two-dimensional system in oblique seas. The details of the solution are shown in the Appendix. At the gap centre, the free-surface elevation corresponding to (1, 0) mode is much more pronounced than in higher modes. The frequency of the predominant peak moves gradually to the low-frequency region as l increases, which is owing to the increase in the inertia of the entrapped fluid. In addition, the predominant peak gets gradually more apparent as l increases. The two-dimensional solution is characterised by a single peak at the (1, 0) mode. As shown in Fig. 17, the application of a two-dimensional solution obviously overestimates the peak response within the gap.

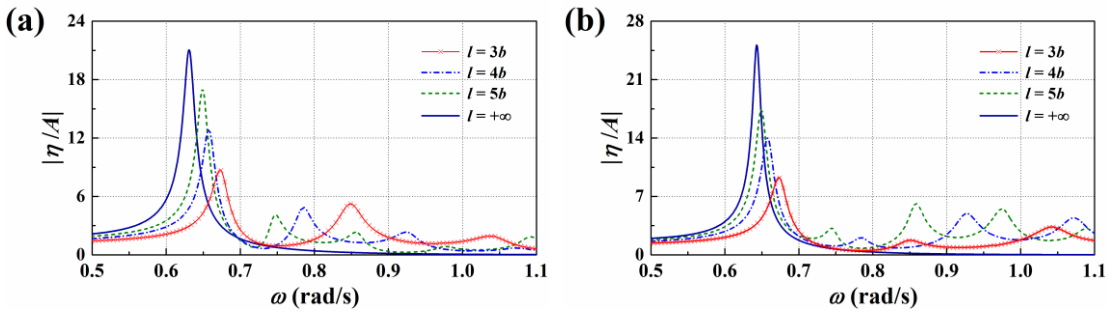

Fig. 17. Variation of the free-surface elevation amplitude at the gap centre (0, 0) under different gap lengths with e = 4.6 m and b = 46 m for the case of a rectangular barge: (a) β = 7.5°, and (b) β = 15°.

We then consider the case that a Wigley hull is alongside a vertical wall. Figs. 18-19 show the variation of the free-surface elevation amplitude at the featured points P_1 to P_4. For the purpose of comparison, the results for a rectangular barge have also been added to these figures. Compared with the case of a rectangular barge, the results for a Wigley hull oscillates less frequently with respect to the wave frequency, and the peak response is much less obvious. Figs. 20-21 shows the distribution of the free-surface elevation amplitude around a Wigley hull in front of a vertical wall for the first three peak frequencies at P_3 and P_4 when β = 30°. The free-surface elevation in the gap is characterised by one single peak. The apparent peak appears around the stern area in long waves, and then moves gradually to the gap centre and gets gradually less evident as the frequency increases. As shown Figs. 20-21, the hydrodynamic interference effect between the Wigley hull and the vertical wall can give rise to the apparent amplification of the free-surface elevation in the gap. However, such amplification is much less obvious when compared with the resonant response for a rectangular barge. The above results show that the hull geometry imposes a significant impact on the free-surface response. The application of a rectangular barge, which is a simple presentation of the complex hull geometry, would obviously overestimate the response in the gap.

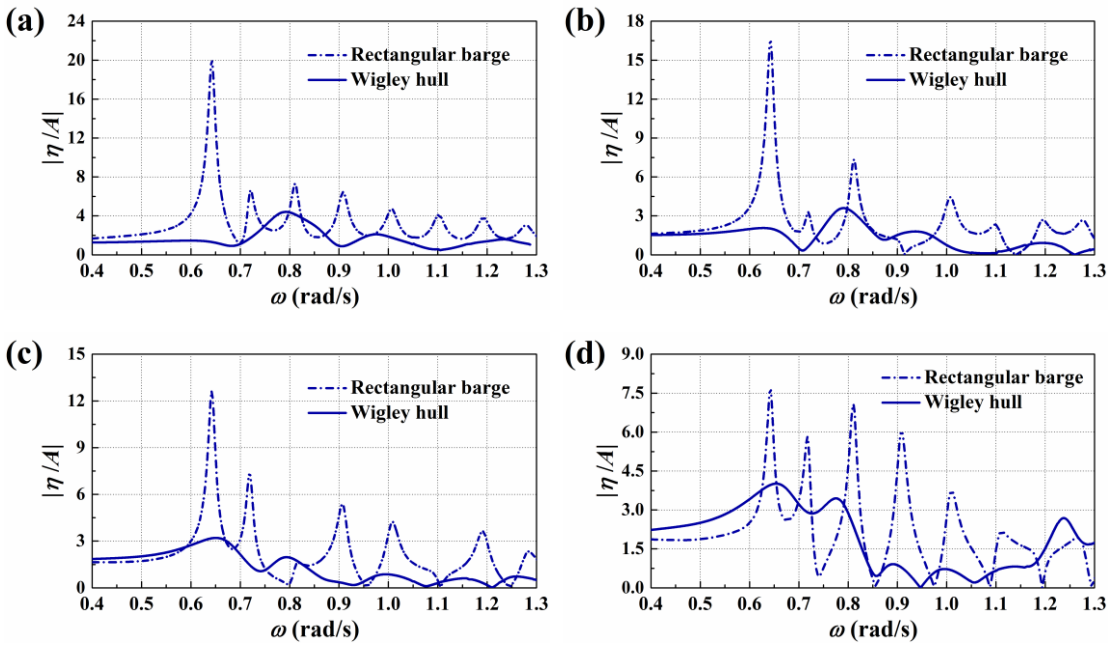

Fig. 18. Comparison of the free-surface elevation amplitude at the featured points P_1 to P_4 for the cases of a rectangular barge and a Wigley hull alongside a vertical wall with e = 4.6 m and β = 0°: (a) P_1, (b) P_2, (c) P_3, and (d) P_4

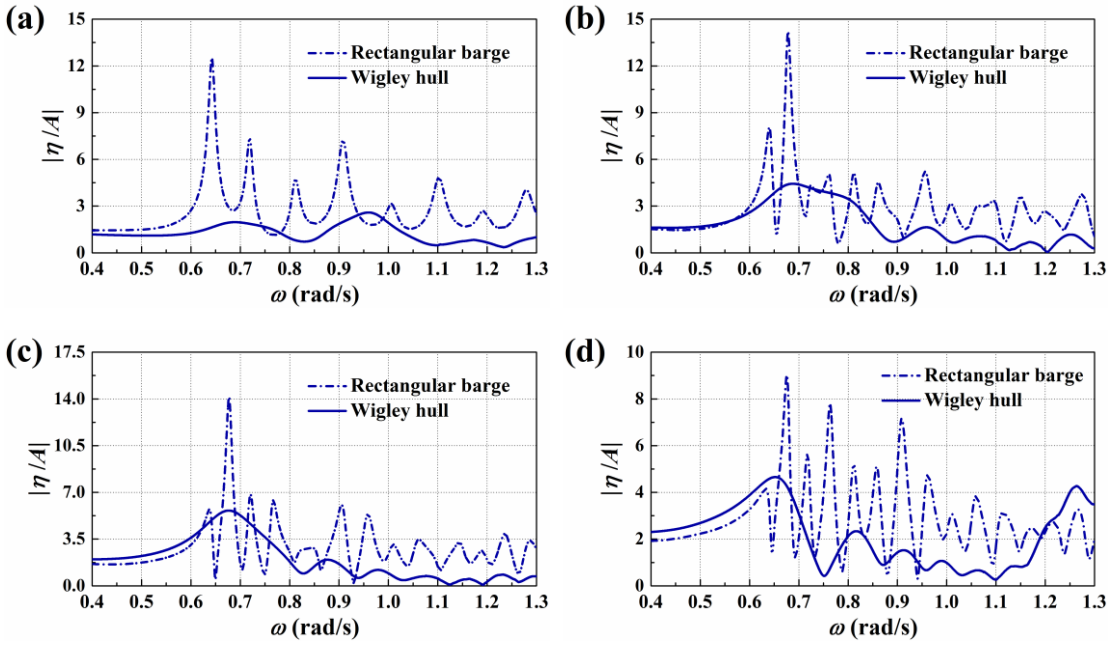

Fig. 19. Comparison of the free-surface elevation amplitude at the featured points P_1 to P_4 for the cases of a rectangular barge and a Wigley hull alongside a vertical wall with e = 4.6 m and β = 30°: (a) P_1, (b) P_2, (c) P_3, and (d) P_4

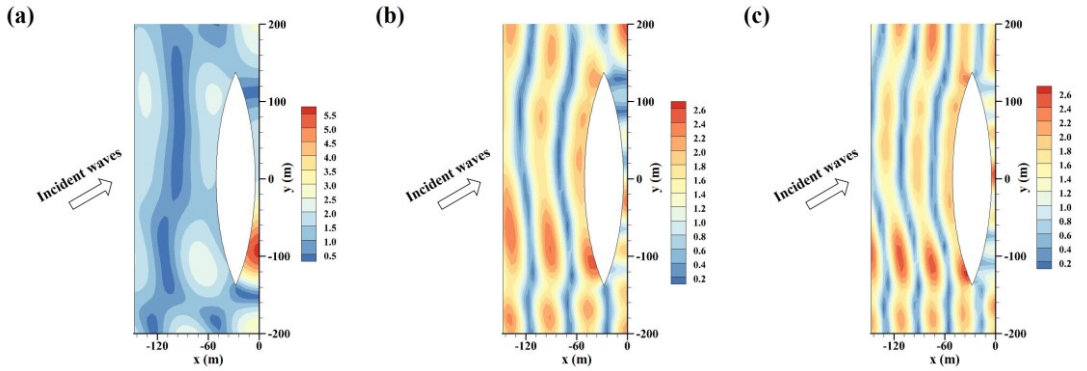

Fig. 20. Distribution of the free-surface elevation amplitude in the vicinity of a Wigley hull in front of a vertical wall when $\beta = 30°$ for the first three peak frequencies at P_3: (a) $\omega = 0.677$ rad/s, (b) $\omega = 0.877$ rad/s, and (c) $\omega = 0.979$ rad/s.

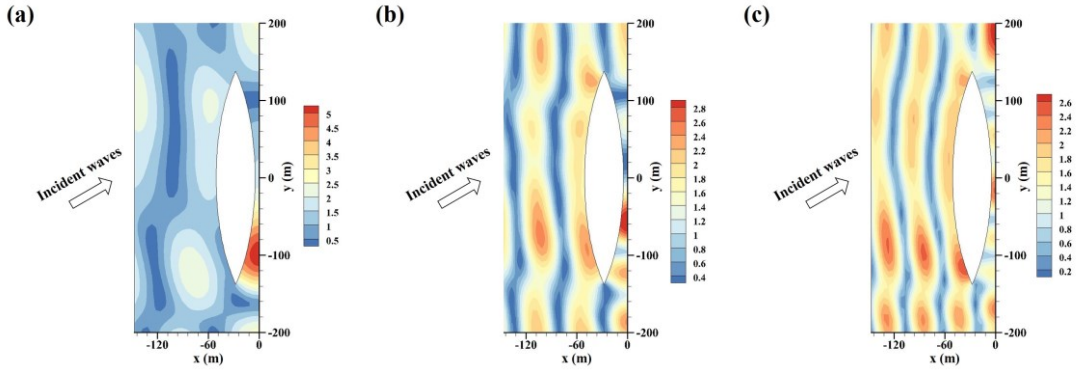

Fig. 21. Distribution of the free-surface elevation amplitude in the vicinity of a Wigley hull in front of a vertical wall when $\beta = 30°$ for the first three peak frequencies at P_4: (a) $\omega = 0.652$ rad/s, (b) $\omega = 0.816$ rad/s, and (c) $\omega = 0.912$ rad/s.

5.2 Linear wave force

The variation of the linear wave force and moment amplitude with respect to the wave frequency is shown in Fig. 22 for the case of a rectangular barge. The pronounced free-surface response in the gap is accompanied by the greatly amplified hydrodynamic pressure. Consequently, the (1, 0) resonant mode causes the apparent amplification of the lateral and vertical wave force. An exception is found from f_y, as f_y is mainly induced by the wave action in the area outside the gap. The pitch moment follows a similar trend as the lateral wave force. In the meantime, significant peaks of the roll and yaw moment are attained at the location of (2, 0) resonant mode, which is caused by the obvious peak in one half region and the obvious trough that appears simultaneously in the remaining half region along the gap.

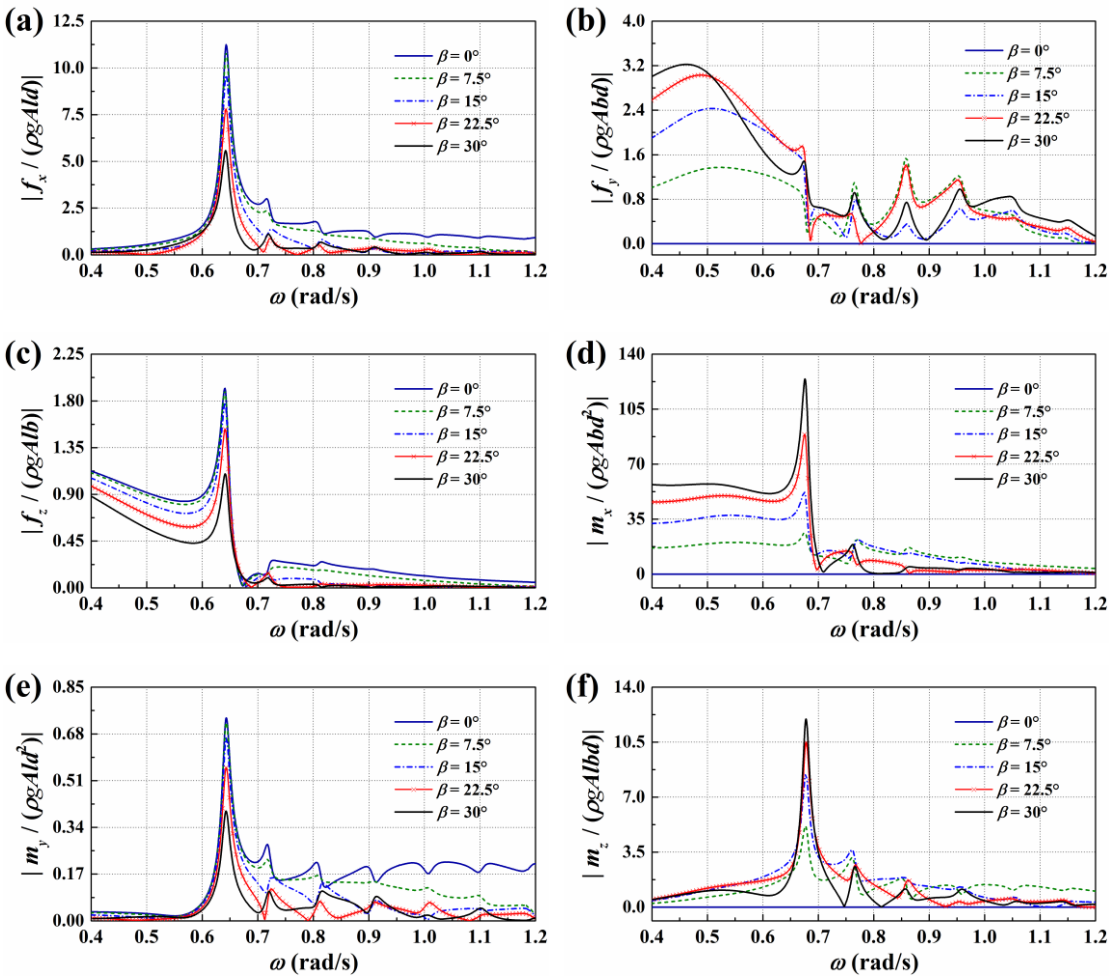

Fig. 22. Variation of the wave force and moment on a rectangular barge in front of a vertical wall with e = 4.6 m: (a) f_x, (b) f_y, (c) f_z, (d) m_x, (e) m_y, and (f) m_z

Analogous results to those in Fig. 22 but with the spacing e = 9.2 m are shown in Fig. 23. The comparison of the results with e = 4.6 m and 9.2 m illustrates that an increase in the spacing moves the frequency of the apparent peak to the high-frequency region and causes a reduction of the peak force or moment, which is consistent with the free-surface elevation.

The results of the wave force and moment on the rectangular barge are then compared with those for a Wigley hull. As shown in Fig. 24, the entrapped waves within the gap can give rise to the enhancement of the wave force and moment on the Wigley hull. However, such enhancement is much less obvious than that for a rectangular barge. An exception can be found from the pitch moment m_y. This is owing to that the entrapped waves around the stern have a large moment arm for the pitch moment on the vessel.

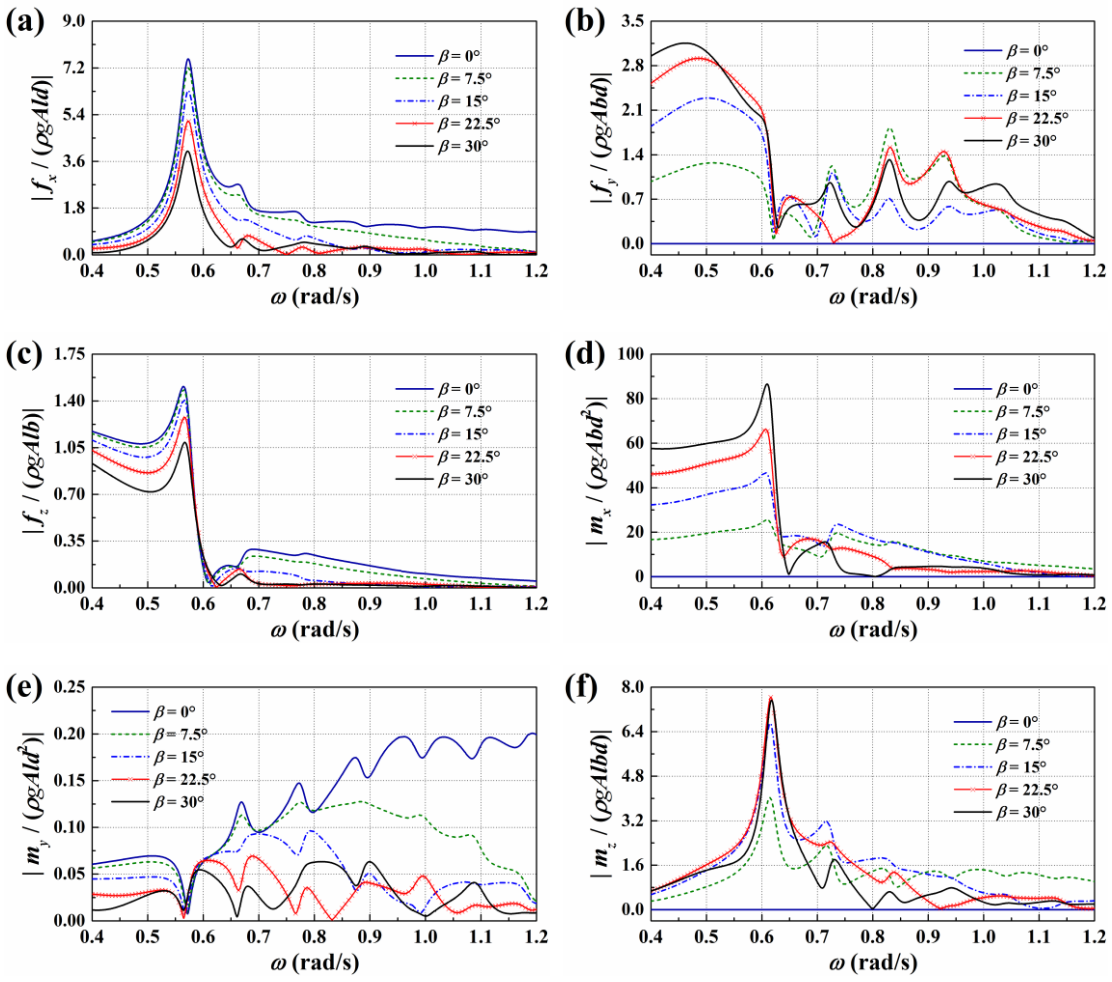

Fig. 23. Variation of the wave force and moment on a rectangular barge in front of a vertical wall with e = 9.2 m: (a) f_x, (b) f_y, (c) f_z, (d) m_x, (e) m_y, and (f) m_z

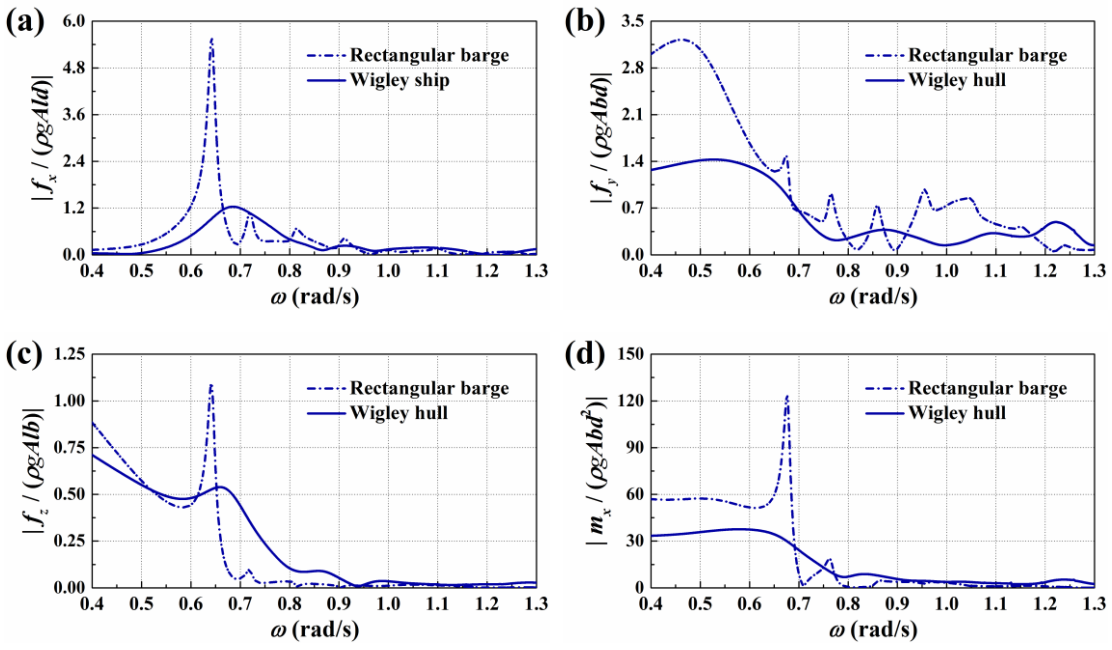

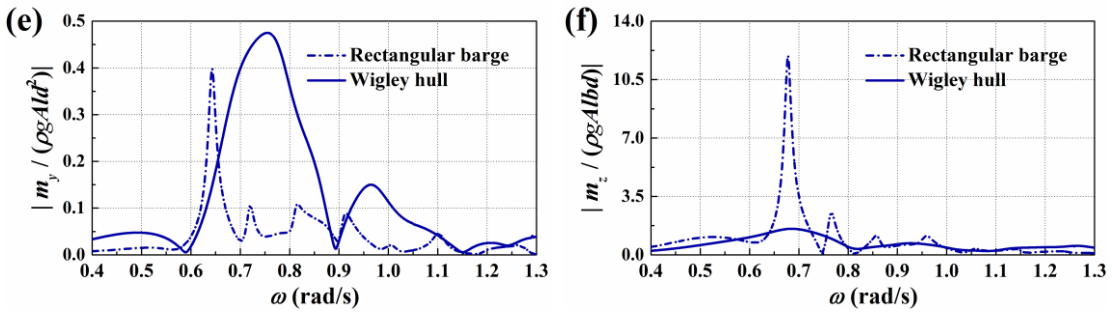

Fig. 24. Comparison of the wave force and moment on a rectangular barge and a Wigley hull in front of a vertical wall with e = 4.6 m and β = 30°: (a) f_x, (b) f_y, (c) f_z, (d) m_x, (e) m_y, and (f) m_z

5.3 Mean wave drift force

The variation of the mean wave drift force and moment are shown in Fig. 25 for the case of a rectangular barge with e = 4.6 m. As illustrated in Fig. 25(a), the mean wave drift force $\bar{f}_x$ is characterised by the remarkably enhanced negative mean force at the resonant frequency of mode (1, 0), i.e., ω_{10}. Under oblique wave action ($\beta > 0$), obvious negative mean force, which tends to push the barge away from the vertical wall, can be attained around the resonant frequencies of both odd and even modes. With the increase of β, the nearly standing wave motion within the gap corresponding to mode (1, 0) gets gradually less obvious, which weakens the pronounced negative mean force at ω_{10}. As β grows to $\pi/6$, the peak corresponding to mode (2, 0) gets more apparent than that of mode (1, 0).

As illustrated in Fig. 25(b), the mean wave force $\bar{f}_y$ is much smaller in magnitude when compared with $\bar{f}_x$, which is due to the small projection area of wave action on the barge along the y-axis. The effect of the resonant fluid motion on $\bar{f}_y$ is not obvious, which is due to that $\bar{f}_y$ is mainly induced by the wave action in the area away from the resonant region.

As shown in Fig. 25(c), the (1, 0) resonant mode can result in an evident positive mean yaw moment, which can cause a mean offset rotation angle of the barge in the horizontal plane along the anti-clockwise direction. This can pull the stern of the barge, which faces the incident waves, closer to the wall, while pushing the bow away from the wall. The enhancement of the mean yaw moment can also be found at higher-order

even or odd modes, but is much less obvious than that at mode (1, 0).

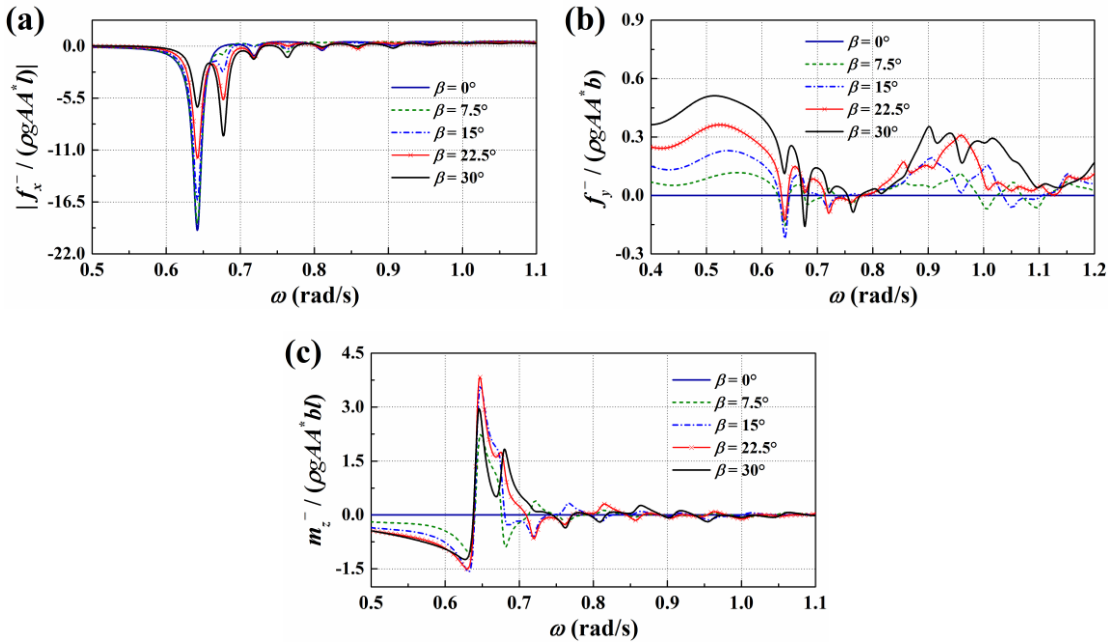

Fig. 25. Variation of the mean wave drift force and moment on a rectangular barge in front of a vertical wall with e = 4.6 m: (a) f_x^-, (b) f_y^-, and (c) m_z^-

Analogous results to those in Fig. 25 but with the spacing e = 9.2 m are shown in Fig. 26. The comparison between the results with e = 4.6 m and 9.2 m illustrates that the enhancement of the mean wave force and moment gets gradually less obvious as the spacing increases.

In Fig. 27, the results of the mean wave drift force and moment on the rectangular barge are compared with those for a Wigley hull. The trend of f_x^- and m_z^- for the case of a Wigley hull differs from that for a rectangular barge. The sharp increment of the negative mean force and positive mean moment induced by the violent fluid motion in the gap cannot be observed from the case of a Wigley hull. The mean force f_y^- on a Wigley hull can be more significant than that on the rectangular barge in a certain frequency range. This is owing to that the entrapped waves around the stern can make a considerable contribution to f_y^- on a Wigley hull.

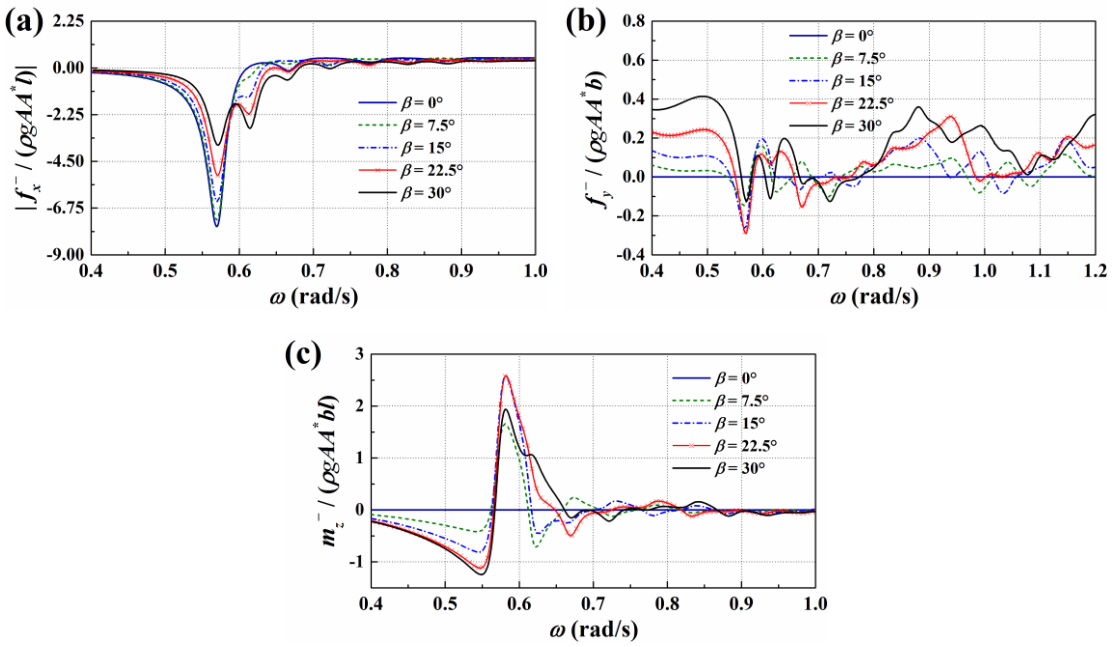

Fig. 26. Variation of the mean wave drift force and moment on a rectangular barge in front of a vertical wall with e = 9.2 m: (a) f_x^-, (b) f_y^-, and (c) m_z^-

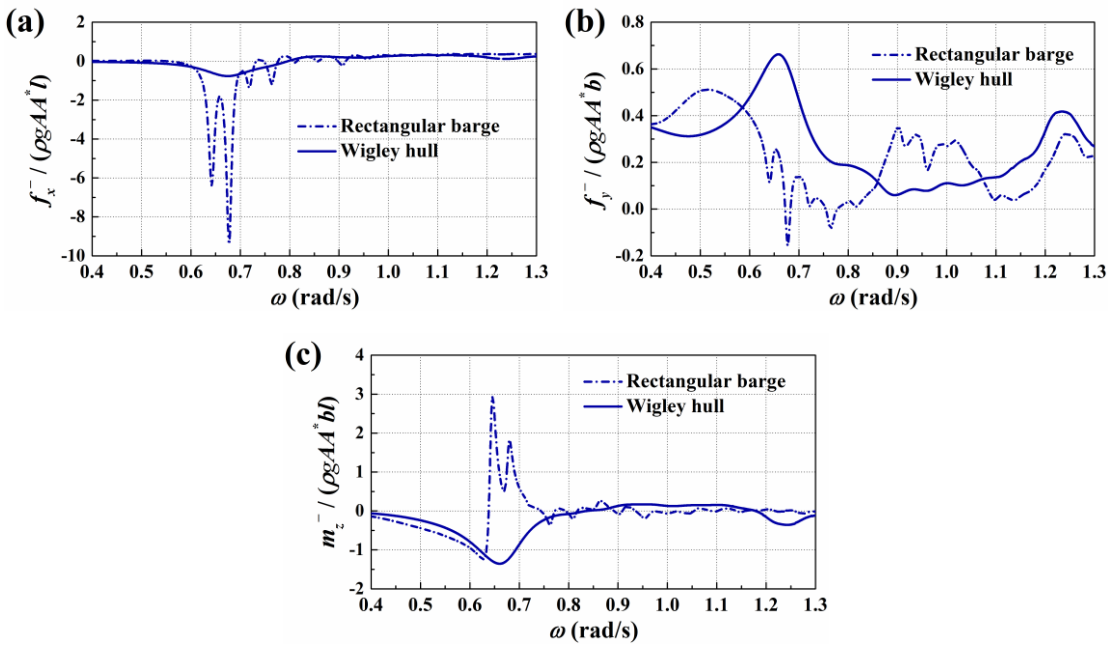

Fig. 27. Comparison of the mean wave drift force and moment on a rectangular barge and a Wigley hull in front of a vertical wall with e = 4.6 m: (a) f_x^-, (b) f_y^-, and (c) m_z^-

6. Conclusions

The focus of this work was on the wave interaction with a vessel alongside a vertical wall in both normal and oblique seas. For a three-dimensional system, this work was

671 conducted using a HOBEM-based numerical model, where the imaging principle was
672 applied to transform the original problem into an equivalent one in open seas. For a
673 two-dimensional system, the eigenfunction expansion matching method has been used.
674 Detailed numerical studies have been conducted. The main conclusions of this research
675 were summarised as follows:

676 1) Different methods have been developed for the calculation of the mean wave drift
677 force on the vessel. A close agreement between the results based on different methods
678 has been obtained. The validity of the present solution was further examined through a
679 comparison with published semi-analytical results. The comparison confirms a
680 favourable consistency with the published data.

681 2) Due to the symmetry of the barge-wall system, only the odd resonant modes can
682 be induced in beam seas ($\beta = 0$). However, under oblique wave action, both the odd and
683 even modes can be induced within the gap formed by a rectangular barge and a long
684 wall. The mode shapes are characterized by the alternative occurrence of apparent peaks
685 and troughs along the gap, which in turn forms the nearly standing wave motion within
686 the gap.

687 3) For the case of a rectangular barge, the apparent peaks of the free-surface elevation
688 amplitude corresponding to different wave headings are not identical. An increase of β
689 can cause a shift of the peak frequencies, which is more evident for lower resonant
690 modes. In addition, the pronounced free-surface elevation corresponding to the (1, 0)
691 resonant mode at the gap centre gets gradually less obvious as β increases. The research
692 also revealed that the application of a two-dimensional solution would overestimate the
693 free-surface response at the gap centre.

694 4) The (1, 0) resonant mode can give rise to the apparent amplification of the lateral
695 and vertical wave force on the rectangular barge. In the meantime, significant peaks of
696 the roll and yaw moment are attained at the location of the (2, 0) resonant mode, which
697 is caused by the simultaneous appearance of the obvious peak in one half region and
698 the obvious trough in the remaining half region along the gap.

699 5) Both the odd and even resonant modes can give rise to the apparent amplification

of the negative mean force on the rectangular barge along the transverse direction, which tends to push the barge away from the wall. In oblique seas, the (1, 0) resonant mode can cause the significant positive mean yaw moment on the barge, which tends to pull the stern of the barge (that faces the incident waves) closer to the wall, while pushing the bow away from the wall. Such enhancement is much less obvious at higher resonant modes.

6) For the case of a Wigley hull, the hydrodynamic interference effect between the Wigley hull and the vertical wall can give rise to a significant free-surface response around the stern area in long waves. The entrapped waves move gradually to the gap centre and get gradually less evident as the wave frequency increases. In addition, for the case of a Wigley hull, the amplification of the free-surface response is much less obvious when compared with the resonant response for a rectangular barge. It suggests that the hull geometry imposes a significant impact on the resonant waves in the gap. The application of a rectangular barge, which is a simple presentation of the complex hull geometry, may obviously overestimate the free-surface response in the gap.

Acknowledgements

The work is financially supported by the National Natural Science Foundation of China (Grant No, 51879039).

Appendix: Solutions to oblique wave interaction with a two-dimensional barge-wall system

We then assume the barge length to be infinitely long compared with the barge width. Then, the original problem in Fig. 1(a) can be approximated by a two-dimensional one as shown in Fig. A1. A train of plane waves of amplitude A and angular frequency ω is obliquely incident upon the barge from $x = -\infty$. The wave heading is β with respect to the positive x-axis. The coordinate system is also shown in Fig. A1.

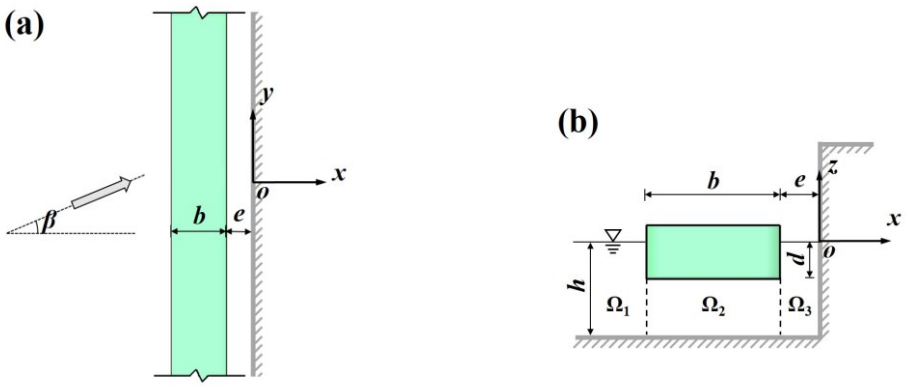

727 Fig. A1 Definition of the coordinate system for a two-dimensional barge–wall system
728

729 Frequency-domain analysis is then conducted. The velocity potential is expressed in
730 the following form:

731 $$\phi = \psi \mathrm{e}^{\mathrm{i}ky\sin\beta}. \tag{A1}$$

732 After inserting Eq. (A1) into the Laplace equation, we can have

733 $$\frac{\partial^2\psi}{\partial x^2} + \frac{\partial^2\psi}{\partial z^2} - \left(k\sin\beta\right)^2\psi = 0. \tag{A2}$$

734 In addition, the boundary conditions satisfied by ψ are as follows:

735 $$\frac{\partial\psi}{\partial x} = 0, \quad \text{on } -d \le z \le 0 \text{ and } x = -b-e; \tag{A3a}$$

736 $$\frac{\partial\psi}{\partial x} = 0, \quad \text{on } -d \le z \le 0 \text{ and } x = -e; \tag{A3b}$$

737 $$\frac{\partial\psi}{\partial z} = 0, \quad \text{on } z = -d \text{ and } -b-e \le x \le -e, \tag{A3c}$$

738 $$\frac{\partial\psi}{\partial x} = 0, \quad \text{on } x = 0, \tag{A4}$$

739 $$\frac{\partial\psi}{\partial z} = 0, \quad \text{on } z = -h, \tag{A5}$$

740 $$\frac{\partial\psi}{\partial z} = \frac{\omega^2}{g}\psi, \quad \text{on } z = 0, \tag{A6}$$

741 and

742 $$\lim_{x\to-\infty}\left[\frac{\partial\left(\psi-\psi_I\right)}{\partial x} + \mathrm{i}k\cos\beta\left(\psi-\psi_I\right)\right] = 0, \tag{A7}$$

743 where

744 $$\psi_I = -\frac{\mathrm{i}Ag}{\omega}\frac{\cosh\left[k\left(z+h\right)\right]}{\cosh\left(kh\right)}e^{\mathrm{i}kx\cos\beta}. \tag{A8}$$

The eigenfunction expansion matching method is then used to obtain the solution to the above-defined boundary value problem. The fluid domain is divided into three sub-domains, which are defined as Ω_1, Ω_2 and Ω_3, respectively, as indicated in Fig. A1. The velocity potentials in Ω_1, Ω_2 and Ω_3 are denoted by ψ_1, ψ_2 and ψ_3, respectively. By using the method of separation of variables, the spatial potential can be expressed in the form of orthogonal series in each subdomain

$$\psi_1(x,\,z)=\psi_I(x,\,z)+\sum_{m=0}^{\infty}\left[R_m\mathrm{e}^{\mu_m x}U_m(\kappa_m z)\right]; \tag{A9a}$$

$$\psi_2(x,\,z)=\sum_{m=0}^{\infty}\left\{\left[B_m p_m(\gamma_m x)+C_m q_m(\gamma_m x)\right]Y_m(\lambda_m z)\right\}; \tag{A9b}$$

$$\psi_3(x,\,z)=\sum_{m=0}^{\infty}\left[D_m\left(e^{\mu_m x}+e^{-\mu_m x}\right)U_m(\kappa_m z)\right], \tag{A9c}$$

where R_m, B_m, C_m and D_m are unknown coefficients; $U_m(\kappa_m z)$ and $Y_m(\lambda_m z)$ are orthonormal functions given at the intervals $[-h,\,0]$ and $[-h,\,-d]$, respectively, and defined as

$$U_m(\kappa_m z)=\frac{\cos\left[\kappa_m(z+h)\right]}{\cos(\kappa_m h)},\quad m\geq 0; \tag{A10a}$$

$$Y_m(\lambda_m z)=\begin{cases}\dfrac{\sqrt{2}}{2}, & m=0,\\ \cos\left[\lambda_m(z+h)\right], & m\geq 1;\end{cases} \tag{A10b}$$

the functions $p_m(\gamma_m x)$ and $q_m(\gamma_m x)$ are defined by

$$p_m(\gamma_m x)=\mathrm{e}^{-\gamma_m x}+\mathrm{e}^{\gamma_m x}; \tag{A11a}$$

$$q_m(\gamma_m x)=\mathrm{e}^{-\gamma_m x}-\mathrm{e}^{\gamma_m x}. \tag{A11b}$$

When $\beta = 0$, $p_m(\gamma_m x)$ and $q_m(\gamma_m x)$ are replaced by 1 and x, respectively. In Eqs. (A10) and (A11), $\kappa_0=-\mathrm{i}k$, and κ_m ($m \geq 1$) represents the mth positive real root of $-\omega^2=g\kappa_m\tan(\kappa_m h)$; λ_m are defined as $\lambda_0=1$ and $\lambda_m=m\pi/(h-d)$ for $m \geq 1$; the eigenvalues μ_m and γ_m are defined as

$$\mu_m = \begin{cases} -\mathrm{i}k\cos\beta, & m = 0, \\ \sqrt{\kappa_m^2 + (k\sin\beta)^2}, & m \geq 1; \end{cases} \tag{A12a}$$

$$\gamma_m = \begin{cases} k\sin\beta, & m = 0, \\ \sqrt{\lambda_m^2 + (k\sin\beta)^2}, & m \geq 1. \end{cases} \tag{A12b}$$

The expressions developed in Eq. (A9) satisfy Laplace's equation and the boundary conditions in Eqs. (A3c), (A4), (A5), (A6) and (A7). In addition, these expressions have to satisfy the condition of the continuity of pressure and normal velocity at the borders between the neighbouring subdomains. To obtain the solutions of the coefficients, the infinite series in Eq. (A9) has to be truncated and only the first M terms are taken. The continuity of normal velocity between different subdomains at $x = -e$ and $x = -b - e$ can be satisfied over the z interval in a least-square manner by using the orthogonal properties of vertical eigenfunctions. The procedure gives the following two sets of equations

$$\begin{aligned} & R_n - \sum_{m=0}^{+\infty} \left\{ \frac{\gamma_m \left[B_m p_m'(\gamma_m x) + C_m q_m'(\gamma_m x) \right]}{\mu_n \mathrm{e}^{\mu_n x} N_n(\kappa_n h)} \cdot \int_{-h}^{-d} Y_m(\lambda_m z) U_n(\kappa_n z)\,\mathrm{d}z \right\} \\ & = -\frac{\mathrm{i}k\cos\beta}{\mu_n \mathrm{e}^{\mu_n x} N_n(\kappa_n h)} \cdot \int_{-h}^{0} \psi_I(x, z) U_n(\kappa_n z)\,\mathrm{d}z, \quad \text{at } x = -b - e; \end{aligned} \tag{A13a}$$

$$\sum_{m=0}^{+\infty} \left\{ \frac{\gamma_m \left[B_m p_m'(\gamma_m x) + C_m q_m'(\gamma_m x) \right]}{\mu_n \left(e^{\mu_n x} - e^{-\mu_n x} \right) N_n(\kappa_n h)} \cdot \int_{-h}^{-d} Y_m(\lambda_m z) U_n(\kappa_n z)\,\mathrm{d}z \right\} - D_n = 0, \quad \text{at } x = -e, \tag{A13b}$$

where $N_n(\kappa_n h)$ represents the inner products of the vertical eigenfunction $U_n(\kappa_n z)$, and is defined by

$$N_n(\kappa_n h) = \frac{1}{\cos^2(\kappa_n h)} \frac{h}{2} \left[1 + \frac{\sin(2\kappa_n h)}{2\kappa_n h} \right]. \tag{A14}$$

By matching the potential between different subdomains at $x = -e$ and $x = -b - e$, the following two sets of linear equations can then be obtained

$$\begin{aligned} & \sum_{m=0}^{+\infty} \left[\frac{2R_m \mathrm{e}^{\mu_m x}}{p_n(\gamma_n x)(h-d)} \cdot \int_{-h}^{-d} U_m(\kappa_m z) Y_n(\lambda_n z)\,\mathrm{d}z \right] - \left[B_n + C_n \frac{q_n(\gamma_n x)}{p_n(\gamma_n x)} \right] \\ & = -\frac{2}{p_n(\gamma_n x)(h-d)} \int_{-h}^{-d} \psi_I(x, z) Y_n(\lambda_n z)\,\mathrm{d}z; \quad \text{at } x = -b - e; \end{aligned} \tag{A15a}$$

$$\left[B_n \frac{p_n(\gamma_n x)}{q_n(\gamma_n x)} + C_n\right] - \sum_{m=0}^{+\infty}\left[\frac{2D_m\left(e^{\mu_m x} + e^{-\mu_m x}\right)}{q_n(\gamma_n x)(h-d)} \cdot \int_{-h}^{-d} U_m(\kappa_m z) Y_n(\lambda_n z)\,\mathrm{d}z\right] = 0, \quad \text{at } x = -e. \tag{A15b}$$

We now get $4M$ complex equations and an equal number of unknown coefficients. Solving the system of linear equations gives the unknown coefficients in the orthogonal series, and the free-surface elevation and wave force can be determined. The detailed expressions of the free-surface elevation and wave force are not shown here for brevity.

Reference

1. Bunnik T, Pauw W, Voogt A. Hydrodynamic analysis for side-by-side offloading. In Proceeding of the 19th International Offshore and Polar Engineering Conference (ISOPE 2009), Osaka, Japan, 2009.
2. Chen X B. Middle-field formulation for the computation of wave-drift loads. Journal of Engineering Mathematics, 2007, 59(1): 61-82.
3. Cong P W, Bai W, Teng B, Gou Y. Semi-analytical solution to the second-order wave loads on a vertical cylinder in bi-chromatic bi-directional waves. Ocean Engineering, 2018, 161: 205-220.
4. Cong P W, Chen L F, Gou Y. Hydrodynamic interaction among multiple columns in front of a vertical wall. Ocean Engineering, 2020, 197: 106877.
5. Ding Y F, Walther J H, Shao Y L. Higher-order gap resonance between two identical fixed barges: a study on the effect of water depth. Physics of Fluids, 2022, 34(5): 052113.
6. Eatock Taylor R, Huang J B. Semi-analytical formulation for second-order diffraction by a vertical cylinder in bichromatic waves. Journal of Fluids and Structures, 1997, 11(5): 465-484.
7. Feng X Y, Bai W. Wave resonances in a narrow gap between two barges using fully nonlinear numerical simulation. Applied Ocean Research, 2015, 50: 119-129.
8. Feng X Y, Bai W, Chen X B, Qian L, Ma Z H. Numerical investigation of viscous effects on the gap resonance between side-by-side barges. Ocean Engineering, 2017, 145: 44-58.
9. Faltinsen O M, Rognebakke O F, Timokha A N. Two-dimensional resonant piston-like sloshing in a moonpool. Journal of Fluid Mechanics, 2007, 575: 359-397.

10. Gao J L, He Z W, Zang J, Chen Q, Ding H Y, Wang G. Topographic effects on wave resonance in the narrow gap between fixed box and vertical wall. Ocean Engineering, 2019, 180: 97-107.
11. Gao J L, He Z W, Zang J, Chen Q, Ding H Y, Wang G. Numerical investigations of wave loads on fixed box in front of vertical wall with a narrow gap under wave actions. Ocean Engineering, 2020, 206: 107323.
12. Heo K, Kashiwagi M. Numerical study on the second-order hydrodynamic force and response of an elastic body-In bichromatic waves. Ocean Engineering, 2020, 217: 107870.
13. He G H, Jing P L, Jin R J, Zhang W, Zhang J W, Liu T. Two-dimensional numerical study on fluid resonance in the narrow gap between two rigid-connected heave boxes in waves. Applied Ocean Research, 2021, 110: 102628.
14. He Z W, Gao J L, Chen H Z, Zang J, Liu Q, Wang G. Harmonic analyses of hydrodynamic characteristics for gap resonance between fixed box and vertical wall. China Ocean Engineering, 2021, 35(5): 712-723.
15. Jiang S C, Bai W, Tang G Q. Numerical investigation of piston-modal wave resonance in the narrow gap formed by a box in front of a wall. Physics of Fluids, 2019, 31(5): 052105.
16. Jiang S C, Gu Q, Cong P W. Fluid resonance in the narrow gap of a box-wall system under cnoidal wave action. Ocean Engineering, 2021, 238: 109774.
17. Kim M H, Yue D K P. The complete second-order diffraction solution for an axisymmetric body Part 2. Bichromatic incident waves and body motions. Journal of Fluid Mechanics, 1990, 211: 557-593.
18. Kristiansen T, Faltinsen O M. A two-dimensional numerical and experimental study of resonant coupled ship and piston-mode motion. Applied Ocean Research, 2010, 32(2): 158-176.
19. Lee C H. On the evaluation of quadratic forces on stationary bodies. Journal of Engineering Mathematics, 2007, 58(1-4): 141-148.
20. Lu L, Cheng L, Teng B, Zhao M. Numerical investigation of fluid resonance in two narrow gaps of three identical rectangular structures. Applied Ocean Research, 2010, 32(2): 177-190.
21. Lu L, Teng B, Cheng L, Sun L, Chen X B. Modelling of multi-bodies in close proximity under water waves-Fluid resonance in narrow gaps. Science China Physics, Mechanics & Astronomy, 2011, 54(1): 16-25.

22. Lu L, Tan L, Zhou Z B, Zhao M, Ikoma T. Two-dimensional numerical study of gap resonance coupling with motions of floating body moored close to a bottom-mounted wall. Physics of Fluids, 2020, 32(9): 092101.
23. Li Y J, Wang X K. Numerical study of effects of gap and incident wave steepness on water resonance between two rectangular barges. European Journal of Mechanics-B/Fluids, 2021, 86: 157-168.
24. Liu Y J, Falzarano J. A wall damping method to estimate the gap resonance in side-by-side offloading problems. Ocean Engineering, 2019, 173: 510-518.
25. Liu Y, Li H J, Lu L, Tan L. A semi-analytical potential solution for wave resonance in gap between floating box and vertical wall. China Ocean Engineering, 2020, 34(6): 747-759.
26. Liang H, Chen X B. A new multi-domain method based on an analytical control surface for linear and second-order mean drift wave loads on floating bodies. Journal of Computational Physics, 2017, 347: 506-532.
27. Liang H, Chua K H, Wang H C, Choo Y S. Numerical and experimental investigations into fluid resonance in a gap between two side-by-side vessels. Applied Ocean Research, 2021, 111: 102581.
28. Miao G P, Saitoh T, Ishida H. Water wave interaction of twin large scale caissons with a small gap between. Coastal Engineering Journal, 2001, 43(01): 39-58.
29. Milne I A, Kimmoun O, Graham J M R, Molin B. An experimental and numerical study of the resonant flow between a hull and a wall. Journal of Fluid Mechanics, 2022, 930.
30. Molin B, Remy F, Camhi A, Ledoux A. Experimental and numerical study of the gap resonances in-between two rectangular barges. In Proceedings of the 13th Congress of the International Maritime Association of the Mediterranean (IMAM 2009), Istanbul, Turkey, 2009: 12-15.
31. Molin B. On the piston and sloshing modes in moonpools. Journal of Fluid Mechanics, 2001, 430: 27-50.
32. Newman J N. Second-order slowly-varying forces on vessels in irregular waves. In: Proceedings of the International Symposium on the Dynamics of Marine Vehicles on Structures in Waves, University College London, London, 1974.
33. Ning D Z, Zhu Y, Zhang C W, Zhao M. Experimental and numerical study on wave response at

the gap between two barges of different draughts. Applied Ocean Research, 2018, 77: 14-25.

34. Ogilvie T F. Second-order hydrodynamic effects on ocean platforms. In: Proceedings of the International Workshop on Ship and Platform Motions, 1983, Berkeley, USA, pp: 205–265.

35. Pauw W H, Huijsmans R H M, Voogt A. Advances in the hydrodynamics of side-by-side moored vessels. In proceedings of the 26th International Conference on Offshore Mechanics and Arctic Engineering (OMAE 2007), San Diego, California, USA, 2007, 42703: 597-603.

36. Perić M, Swan C. An experimental study of the wave excitation in the gap between two closely spaced bodies, with implications for LNG offloading. Applied Ocean Research, 2015, 51: 320-330.

37. Saitoh T, Araki T, Miao G P, Ishida H. Experimental study on resonance in a narrow gap between modules of very large floating structure. In Proceedings of the Civil Engineering in the Ocean. Japan Society of Civil Engineers, 2003, 19: 595-600.

38. Sun L, Eatock Taylor R, Taylor P H. First-and second-order analysis of resonant waves between adjacent barges. Journal of Fluids and Structures, 2010, 26(6): 954-978.

39. Sun L, Eatock Taylor R, Taylor P H. Wave driven free surface motion in the gap between a tanker and an FLNG barge. Applied Ocean Research, 2015, 51: 331-349.

40. Shao Y L, Zheng Z P, Liang H, Chen J K. A consistent second-order hydrodynamic model in the time domain for floating structures with large horizontal motions. Computer-Aided Civil and Infrastructure Engineering, 2022, 37: 894-914.

41. Tan L, Lu L, Tang G Q, Cheng L, Chen X B. A viscous damping model for piston mode resonance. Journal of Fluid Mechanics, 2019, 871: 510-533.

42. Teng B, Eatock Taylor R. New higher-order boundary element methods for wave diffraction/radiation. Applied Ocean Research, 1995, 17(2): 71-77.

43. Teng B, Ning D Z, Zhang X T. Wave radiation by a uniform cylinder in front of a vertical wall. Ocean Engineering, 2004, 31(2): 201-224.

44. Teng B, Gou Y, Ning D Z. A higher order BEM for wave-current action on structures—direct computation of free-term coefficient and CPV integrals. China Ocean Engineering, 2006, 20(3): 395-410.

45. Teng B, Cong P W. A novel decomposition of the quadratic transfer function (QTF) for the time-

domain simulation of non-linear wave forces on floating bodies. Applied Ocean Research, 2017, 65: 112-128.

46. Wang D G, Zou Z L. Study of non-linear wave motions and wave forces on ship sections against vertical quay in a harbor. Ocean Engineering, 2007, 34(8-9): 1245-1256.
47. Zhao W H, Wolgamot H A, Taylor P H, Eatock Taylor R. Gap resonance and higher harmonics driven by focused transient wave groups. Journal of Fluid Mechanics, 2017, 812: 905-939.
48. Zhao W H, Taylor P H, Wolgamot H A, Eatock Taylor R. Gap resonance from linear to quartic wave excitation and the structure of nonlinear transfer functions. Journal of Fluid Mechanics, 2021, 926.
49. Zhou K, Hu Z Q, Zhao D Y, Meng X Y. Oblique wave effects on the hydrodynamic responses of side-by-side moored FLNG and LNGC. Journal of Waterway, Port, Coastal and Ocean Engineering, 2018, 144(4): 04018007.